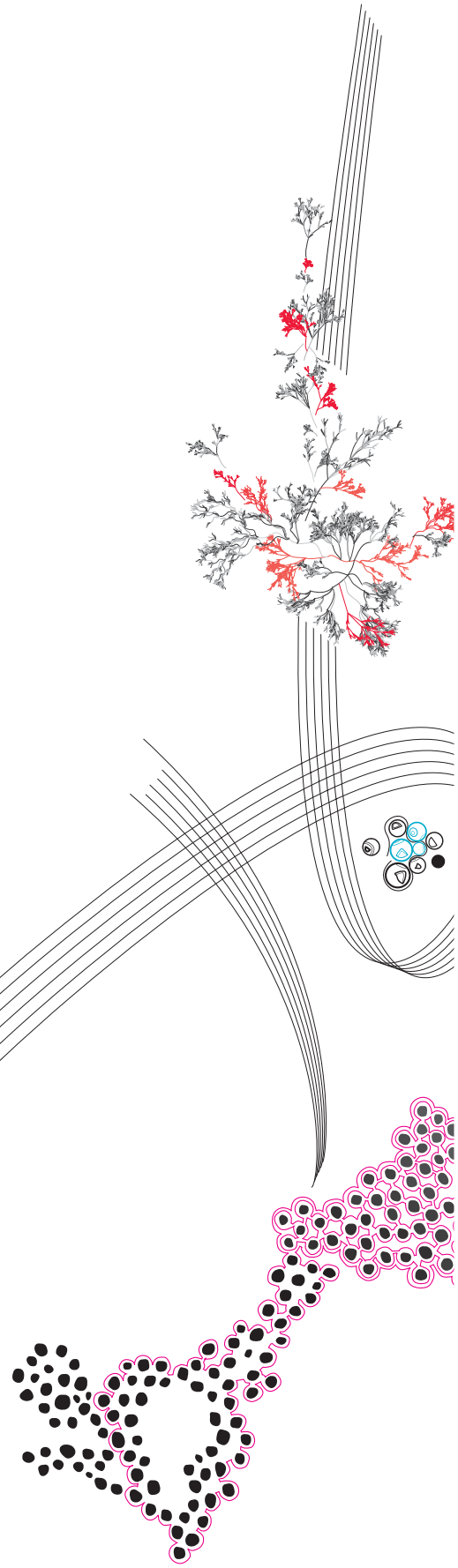

MSc Electrical Engineering

Design and Fabrication of a MEMS-Based Paramagnetic Oxygen Sensor

Dennis Hu

Supervisors:
S. Azadi Kenari MSc
dr.ir. R.J. Wiegerink
prof.dr.ir. M. Odijk
prof.dr.ir. J.C. Lötters

September, 2024

Department of Electrical Engineering
Faculty of Electrical Engineering,
Mathematics and Computer Science

UNIVERSITY OF TWENTE.

Design and Fabrication of a MEMS-Based Paramagnetic Oxygen Sensor

Dennis Hu[1]

September, 2024

[1]Email: d.hu-5@student.utwente.nl

Abstract

The paramagnetic properties of oxygen can be used in sensors to measure the oxygen percentage. MEMS technology could improve conventional paramagnetic oxygen sensors in miniaturisation and fabrication costs. In this thesis assignment, two concepts based on the deflection of flow and magnetic wind have been fabricated in the cleanroom and tested. To this end, a theoretical basis is made for paramagnetic FEM simulations and flow sensor design. Testing of both sensors strongly indicates an oxygen responsivity. There is, however, signal pollution by flow rate sensitivity and yet to be identified sources. Further understanding of the sensor and adjustments to the sensor design are required to accurately measure the oxygen concentration.

Keywords: Paramagnetic Oxygen Sensor, Magnetic Wind, MEMS, Flow Sensor

Contents

Chapter 1

Introduction

1.1 Background

The oxygen concentration is critical for many processes and applications, from internal combustion engines, where the right ratio of fuel to oxygen is needed, to life sciences, where oxygen sensors are used in medical fields or to track fermentation processes [1]. To monitor these processes, oxygen sensors are used, of which a wide variety exists. The sensors can be grouped into a few working principles: electrochemical, solid-state, optical, and paramagnetic.

Electrochemical sensors, such as Galvanic sensors, generate an electrical current by a chemical reaction proportional to the oxygen concentration. Due to their simplicity, cost-effectiveness, and linear response, these sensors are widely used in medical devices and portable gas detectors. However, they face limited response times and a relatively short lifespan of 1 to 2 years [2].

Solid-state sensors, represented by zirconia (ZrO_2) and titanium oxide (TiO_2) sensors, leverage the unique properties of certain ceramics at high temperatures. Zirconia sensors, in particular, have found widespread use in automotive exhaust systems and industrial furnaces, as they are robust in harsh environments. While these sensors excel in high-temperature applications, they require heating and are generally more complex and expensive than their electrochemical counterparts [2].

Optical oxygen sensors represent a more recent innovation in the field. These sensors use the principle of luminescence quenching by oxygen to provide fast, non-consumptive measurements. Their ability to be miniaturized and their immunity to interference from other gases make them ideal for medical diagnostics, food packaging, and biotechnology applications. However, they can be sensitive to environmental factors such as light and temperature, requiring careful calibration and control [1][3].

Electrochemical fuel cell sensors offer a long-term solution for oxygen sensing, particularly in industrial safety and environmental monitoring applications. While more expensive, these sensors provide stable output over extended periods [2].

Paramagnetic oxygen sensors

Paramagnetic oxygen sensors also play a role in the oxygen sensor market. These sensors work based on the paramagnetic material property that is mainly specific to oxygen, making them highly selective in normal air. By manipulating oxygen with magnetic fields, they can accurately measure oxygen concentration.

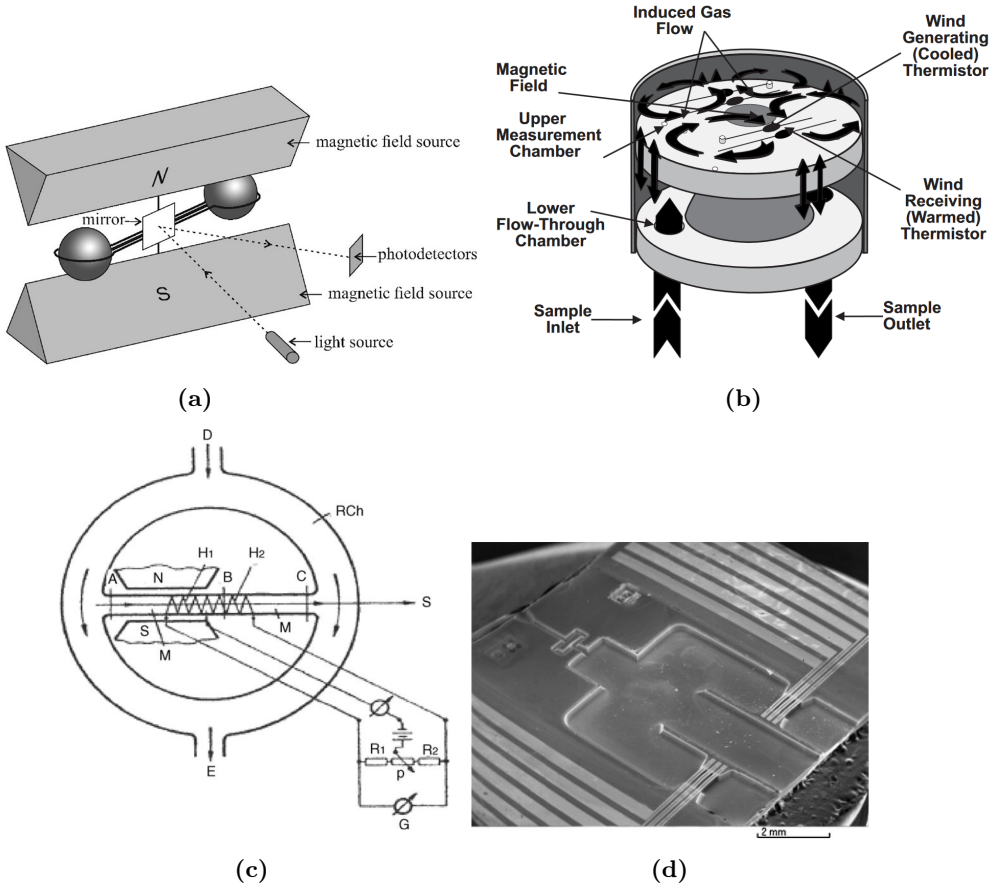

Figure 1.1: *(a) Schematic of the dumbbell sensor concept [4]. (b) Schematic of the XMO2 sensor showing the principle of magnetic wind [5]. (c) Magnetic wind sensor [6]. (d) Fluidic bridge based MEMS paramagnetic oxygen sensor that works based on air deflection proportional to the oxygen concentration [7].*

Examples include the dumbbell as shown in Figure 1.1a, where a dumbbell structure is pivoted in the middle. The dumbbell balls, neutrally buoyant in air, are in the range of a magnetic field. Once oxygen gets attracted to the magnets, air density will slightly change. Being neutrally buoyant, the balls move due to the change in pressure, proportional to the oxygen concentration. This movement is read out by deflecting a light beam from the pivoting point of the dumbbell [4][8].

Another example is the *XMO2* from General Electric, which uses the thermal magnetic wind phenomenon depicted in Figure 1.1b. Because the magnetic property of oxygen decreases with temperature, convection can be created by one side pulling in the air with a magnet and letting it go by heating the other side [5].

However, commercially available paramagnetic oxygen sensors are generally fragile and expensive, and their manufacturing elaborate [4]. This is where MEMS-based sensors can provide a solution; sensor fabrication can be scaled using MEMS fabrication technology, allowing for robust and small sensors.

A few of these paramagnetic sensors have an existing counterpart in MEMS. The dumbbell principle has been demonstrated in MEMS technology [8]. Based on the same principle of the *XMO2*, a concept of a miniaturized oxygen sensor has been worked out in [6]. As shown in Figure 1.1c, the sensor has a gas flow split into two channels from the top to the bottom. Cold air gets pulled in by a magnetic field from the left and can leave the tube

via the warmed-up side by a coil, which is then read out by a Wheatstone bridge. There is no publication yet on a fabricated MEMS device of this type.

Some original ideas could only work on the MEMS scale, such as the paramagnetic deflection sensor, where the amount of deflected gas by a magnet from a primary gas stream is proportional to the oxygen concentration shown in Figure 1.1d [7]. However, none of the experimental MEMS paramagnetic oxygen sensors are commercially available yet [4].

1.2 Research goals

This thesis aims to contribute towards the development of MEMS-based paramagnetic oxygen sensors by providing a proof of concept that leverages existing sensor principles. This will be done for the deflection sensor (Figure 1.1d), where oxygen causes a deflection of flow, and for the magnetic wind phenomenon (Figure 1.1c).

Ultimately, the sensor designs will be fabricated in the cleanroom. To this end, FEM simulations and theoretical analyses of the MEMS sensor designs will be conducted. Simulations will be used to predict sensor behaviour and optimize design parameters. The analysis will contribute towards refining the design.

After the design, prototype MEMS paramagnetic oxygen sensors will be fabricated based on the optimized designs to test their performance using oxygen percentages between 0 vol.% and 20 vol.%. Prototypes will be fabricated using standard MEMS processing techniques. Ultimately, a sensor with a sensitivity and response time comparable to the commercially available sensors is targeted. This means an accuracy of 0.1 vol.% oxygen and a response time from 0 vol.% to 20 vol.% of below 1 second.

1.3 Thesis outline

Beginning with theory, Chapter 2 will cover paramagnetic forces on oxygen and the flow sensor based on hot wires. Based on the theory two sensor concepts are proposed in Chapter 3: a deflection and a magnetic wind based sensor. The realisation and fabrication of these sensors in MEMS technology is covered in Chapter 4. Chapter 5 and Chapter 6 cover the testing methods and materials and the subsequent results and discussion, respectively. Lastly, a conclusion is formed in Chapter 7 with recommendations for further research.

Chapter 2

Theory

This chapter covers the fundamental theory to gain insight into the sensor's behaviour. The theory and models are subsequently used for the sensor's design and simulations. The theory is divided into two sections: the interaction of a paramagnetic gas with a magnetic field and heaters and the theory and model for hot-wire flow sensing.

2.1 Paramagnetism of oxygen

The magnetic properties of materials originate from the magnetic moments of their constituent atoms [9][10]. These magnetic moments arise from the spin angular momentum of electrons, where each electron can be thought of as a tiny loop of current creating a magnetic field. The arrangement of electron spins is governed by quantum mechanical principles, particularly Hund's rule, which provides guidelines for determining the ground state configuration of multi-electron atoms. Electrons occupy orbitals to maximize the total spin quantum number. For a given orbital, the configuration with the largest total orbital angular momentum in one direction is preferred. Figure 2.1 shows the electron orbital filling for oxygen atoms and molecules [4]. The two unpaired spins contribute towards a net magnetic moment in the oxygen molecule, indicating its magnetic properties. However, the net magnetic field of oxygen gas remains zero as their alignment is randomized due to thermal fluctuation.

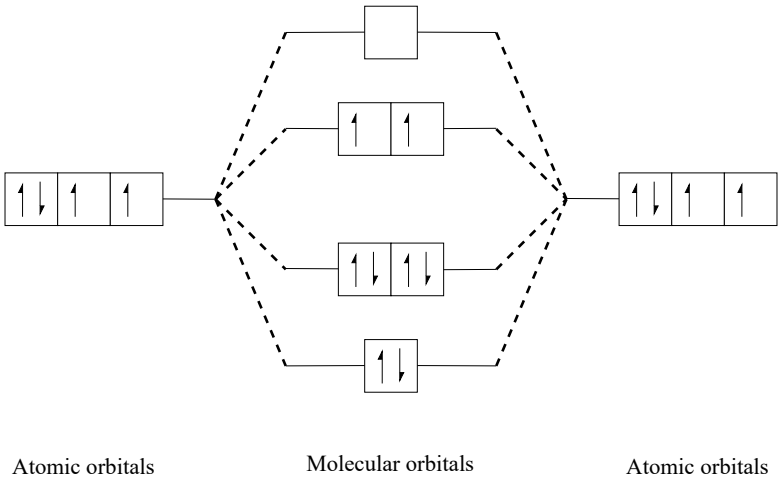

Figure 2.1: *Simplified schematic of the electron spin occupation of the individual oxygen atoms and the oxygen molecule.*

Magnetic susceptibility

Magnetic materials distinguish themselves by reacting to an external magnetic field **H** by creating their own magnetic field, referred to as the magnetization **M**, the magnetic moment per unit volume. The ratio between **H** and **M** is a unitless material property susceptibility $\mathbf{M} = \chi\mathbf{H}$. This field is opposite to the external field for diamagnetics ($\chi < 0$). Paramagnetic and ferromagnetic materials have a field that adds to the total applied field ($\chi > 0$).

The susceptibility is proportional to the number of unpaired electron spins

$$\chi = \frac{N\mu_B^2}{3kT}, \tag{2.1}$$

with the number of particles per volume N, the Bohr magneton μ_B, Boltzmann constant k, and the temperature T [10]. Building upon Curie's law $C = \chi/T$, it shows how χ is inversely proportional to the temperature. This results from an increased difficulty in aligning the molecules with increased thermal energy. On the other hand, a higher pressure increases susceptibility as the density of magnetic dipoles per volume becomes larger [9]. The dependencies on temperature and pressure have been modelled using

$$\chi = \chi_0 \frac{PT_0^2}{P_0T^2} y \tag{2.2}$$

where the χ_0 is the susceptibility under the temperature and pressure of T_0, P_0, and y the volume fraction of oxygen [11].

In Table 2.1 various susceptibility values for commonly found gasses in ambient air are shown. Oxygen is the only common gas in the air with a significantly positive susceptibility value. This property is used to monitor oxygen levels selectively. Apart from oxygen, nitric oxide (NO) and nitrogen dioxide (NO_2) also have a relatively high susceptibility, but their presence in normal air is negligible.

Table 2.1: *Susceptibility values of various gasses [4].*

Gas	N_2	O_2	Ar	CO_2	NO	NO_2
Susceptibility χ $[10^{-10}]$	-42.28	6880	-97.07	-116.2	5510	864.9

Paramagnetic volume force

Aligning the magnetic dipoles requires work. When no external field is applied, the net magnetic moment is 0 due to thermal fluctuations. Increasing **H** starts to align the dipoles, and the subsequently rising **M** stores potential energy in the alignment of the magnetic dipoles [9]. The change in potential energy can be expressed as

$$dW = -\mu_0 \mathbf{H} \cdot d\mathbf{M} \tag{2.3}$$

with the magnetic permeability μ_0. The energy can be found by integrating work over the change in magnetization. For linear, isotropic, and homogeneous (LIH) magnetic materials, **M** increases proportionally to **H** with susceptibility χ or $\mathbf{M} = \chi\mathbf{H}$ [9]. This results in

$$W = -\mu_0 \int_0^M \mathbf{H} \cdot d\mathbf{M} = -\mu_0 \int_0^M \frac{1}{\chi}\mathbf{M} \cdot d\mathbf{M} = -\frac{1}{2}\mu_0 \mathbf{H} \cdot \mathbf{M}. \tag{2.4}$$

The equation shows that aligning the magnetization with the externally applied field minimizes the system's energy state. The volume force can be found by looking at the gradient of the potential energy

$$\mathbf{F} = -\nabla W = \nabla \left[\frac{1}{2}\mu_0 \mathbf{H} \cdot \mathbf{M}\right] \tag{2.5}$$

where the force is in the direction of minimizing energy. Substituting $\mathbf{M} = \chi\mathbf{H}$ into eq. (2.5) and rearranging all constants results in

$$\mathbf{F} = \frac{1}{2}\mu_0 \chi \nabla \mathbf{H}^2. \tag{2.6}$$

Rewriting equation 2.6 in $\mathbf{B}$ can be done assuming

$$\mathbf{B} = \mu_0(\mathbf{H} + \mathbf{M}) = \mu_0 \mathbf{H}(1 + \chi) \approx \mu_0 \mathbf{H}. \tag{2.7}$$

This holds as paramagnetic susceptibility is very small ($\chi \ll 1$), in the range of $10^{-5} - 10^{-3}$ [9]. Substituting eq. (2.7) into eq. (2.6) then yields

$$\mathbf{F}_\mathrm{V} = \frac{\chi}{2\mu_0}\nabla \mathbf{B}^2. \tag{2.8}$$

This states that the force points towards an increasing magnetic field, where the steeper gradient in the field creates a larger force independent of polarity.

Gas Dynamics of Oxygen in Air Under Magnetic Force

Due to gas dynamics at the molecular level, the air mixture tends to move when only the oxygen fraction in air experiences a volume force. In typical atmospheric conditions, gas molecules undergo frequent collisions. For air at room temperature, the collision frequency is $7.9 \cdot 10^9$ collisions per second with a mean free path of 68 nm.

When magnetic forces accelerate paramagnetic oxygen molecules, they collide with other air components, primarily nitrogen. These collisions result in energy and momentum transfer. The time scale of this energy transfer is much shorter than the time scale of macroscopic gas movement. It should, therefore, be reasonable to approximate the air mixture as a whole with a volume force proportional to the volume fraction of oxygen present as has been done in [4].

2.2 Hot wire

Hot wires will be used as a sensor to measure the flow of gasses due to their paramagnetic interactions with oxygen. To better understand the mechanics of these wires, the temperature of the wire and the temperature flow dependance will be examined.

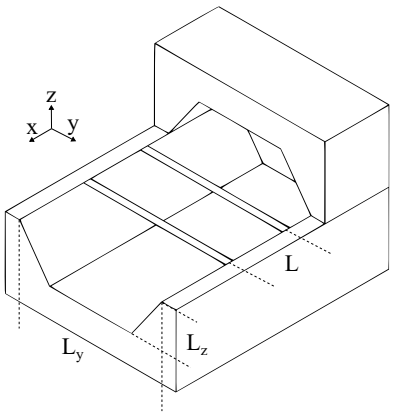

Figure 2.2: *Schematic cross-section showing the hexagonal channel with two wires crossing.*

The temperature of the wire is the result of a heat or energy balance. Figure 2.2 shows a schematic of the wire. The input energy is provided by joule heating using a direct current over a resistance. Heat losses can occur via various mechanisms. A large fraction of the losses will be in the form of conduction, either to the surrounding fluid or at the attachment points of the wire. Another form of heat loss is via convection, where a moving fluid mass carries heat away from the wire. Radiative losses in conventional MEMS for similar structures will be negligible compared to other losses and, therefore, omitted [12][13].

Following the derivation by Bruun [13] of a comprehensive hot wire model, the heat balance for a segment dy along the beam can be expressed as

$$-k_w A_w \frac{\partial^2 T_w}{\partial y^2} + \pi d h T_o = \frac{I^2 R_w}{A_w} \tag{2.9}$$

with the beam thermal conductivity k_w, beam crossectional area A_w, the wire overheat temperature T_o, the difference between the ambient and the heated temperature at position y along the wire, characteristic width of the beam d, heat transfer coefficient h, wire current I, and wire resistance at fluid temperature R_a. The first term represents the conductive changes in the beam's temperature, resulting in sidewall losses. The second term models the heat transfer to outside the wire, and the third term is the joule heat generation.

As the wire's resistivity R_w is also temperature dependent with $R_w = R_a(1 + \alpha T_o)$ it can be substituted and reordered as

$$-k_w A_w \frac{\partial^2 T_w}{\partial y^2} + \pi d h T_o = \frac{I^2}{A_w} R_a (1 + \alpha T_o), \tag{2.10a}$$

$$-k_w A_w \frac{\partial^2 T_w}{\partial y^2} + \left[\frac{I^2 R_a \alpha}{A_w} + \pi d h \right] T_o = \frac{I^2 R_a}{A_w}. \tag{2.10b}$$

The energy balance of the wire can be written as the homogenous second-order differential equation

$$\frac{d^2T_o}{dy^2} + K_1T_o + K_2 = 0. \tag{2.11a}$$

with

$$K_1 = \frac{I^2\rho_a\alpha}{k_wA_w^2} - \frac{\pi dh}{k_wA_w}, \tag{2.11b}$$

$$K_2 = \frac{I^2\rho_a}{k_wA_w^2}. \tag{2.11c}$$

A solution to this differential equation is found in the form

$$T_o = \frac{K_2}{|K_1|}\left[1 - \frac{\cosh\left(\sqrt{|K_1|}x\right)}{\cosh\left(\sqrt{|K_1|}\frac{l}{2}\right)}\right]. \tag{2.12}$$

The average temperature of the wire can be found integrating eq. (2.10b), which yields

$$T_{o,m} = \frac{K_2}{|K_1|}\left[1 - \frac{\tanh\left(\sqrt{|K_1|}\frac{l}{2}\right)}{\sqrt{|K_1|}\frac{l}{2}}\right]. \tag{2.13}$$

Figure 2.3 shows the changing temperature profile for increasing width over length ratios. As the width relative to the length of the wire increases, the heat conduction to the substrate becomes more significant, decreasing the average temperature.

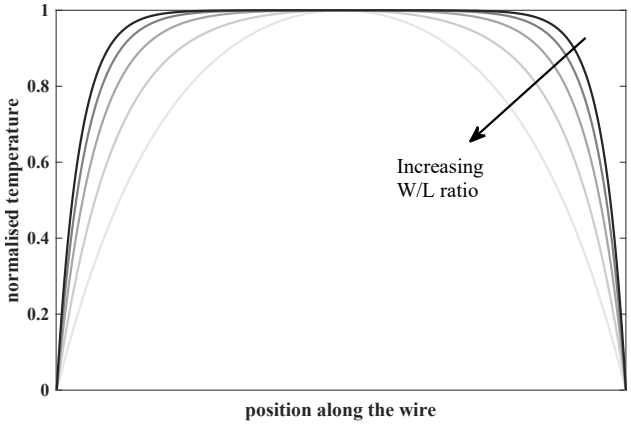

Figure 2.3: *The temperature profile along a heated wire for increasing wire width over length ratios. Temperature curves are normalised to their peak temperature.*

2.3 Hot wire with cross flow

Placing a wire across the channel as depicted in Figure 2.2 allows for anemometric operation; the flow carries heat away from the wire, leading to a temperature drop of the wire and an increase in the temperature of the gas downrange. How well the heat is carried away by the fluid depends on its behaviour.

Flow regimes

Gas flows can behave differently depending on the velocity. A factor in determining the flow behaviour is the ratio of viscous forces to inertial forces within the fluid. Viscosity stabilizes, causing the fluid to flow in smooth, parallel layers—a phenomenon known as laminar flow. However, the flow becomes turbulent when inertial forces overcome this viscous damping. These distinct flow regimes can be differentiated using the Reynolds number (Re), a dimensionless quantity defined as

$$Re = \frac{vD_h}{\nu} \tag{2.14}$$

with the fluid velocity v in $\mathrm{m\,s^{-1}}$, the hydraulic diameter D_h in m, and the kinematic viscosity of the fluid ν in $\mathrm{m^2\,s^{-1}}$.

At the boundary between a fluid and a solid wall, friction causes the fluid velocity to drop to zero, creating a thin boundary layer. The bulk fluid follows the path of least resistance, automatically diverting and increasing its flow away from walls. However, for submicrometer dimensions, this boundary layer decreases as friction decreases. More fluid moves closer to the surface.

The Knudsen number (Kn) can identify the boundary layer regimes. the ratio of the molecular mean free path to the characteristic flow dimension. It defines different flow regimes going from a continuum of flow ($\mathrm{Kn} < 0.001$), where the collisions between gas particles are frequent, flowing cohesively, to molecular flow ($\mathrm{Kn} > 10$), where interactions are scarce.

For most MEMS applications, the Reynolds number will be low enough for laminar flow. The Knudsen number is normally high enough to assume stationary velocity boundary conditions. Flow velocities are also low enough to approximate gas as a non-compressable fluid, as the fluid will redistribute fast enough.

Heat transfer

Heat is primarily lost through conduction and convection. Convective heat transfer depends on the amount of heat carried away by the flow and the amount that the heat can diffuse through the fluid [14]. In the case of no flow, heat will be conducted via the substrate at the wire's endpoints. Ideally, these losses are minimized as they do not contribute to the sensing of the fluid flow. Convective losses are mainly due to the moving fluid carrying away heat or forced convection. In the macroscale hot wires, free convection and air circulation also play a role due to the buoyancy of increased temperature. However, due to the relatively large viscous forces at the microscale, the fluid mainly remains stationary [12].

In the model of Bruun (eq. (2.12)), the flow dependence of the temperature of the wire depends on the heat transfer coefficient h. According to Newton's law of cooling, h relates the heat loss as a flux over the wire's surface area $\dot{Q}$ with the temperature difference ΔT of the wire to the fluid as

$$h = \frac{\dot{Q}}{\Delta T}. \tag{2.15}$$

The coefficient h itself is also a function of the fluid velocity. Commonly, this has been modelled using the King's law approach [12] [15]

$$h = A + Bv^{\frac{1}{n}} \tag{2.16}$$

with the conductive losses represented by A, the convective losses by B and the shape factor n, which is usually found to be around 2 [16]. The values of A and B depend on wire geometry [17]. Nominal values found for hot wire anemometry with gasses range from 5 to 25 $\mathrm{W\,m^{-2}\,K}$ for free convection and 20 to 300 $\mathrm{W\,m^{-2}\,K}$ for forced convection [14].

Temperature distribution along the channel

The temperature distribution along the channel has been modelled by Lammerink [18]. A qualitative adaptation of this model has been made by van Bree [16]. The derivation of the wire's temperature looks similar to that of van Bruun, assuming no heating losses to the substrate and no changes in wire resistance. Lammerink's model estimates the heat transfer coefficient h using an analytical formula, while van Bree uses King's Law with A and B as fitting parameters.

Looking along the x direction in Figure 2.2, the differential equation for the temperature along the channel according to [18] becomes

$$D\frac{\partial^2 T_o}{\partial x^2} - v\frac{\partial T_o}{\partial x} - gDT_o = 0 \tag{2.17}$$

with the thermal diffusivity of the fluid $D = k_f/\rho c_p$, the geometric factor $g = 1/L_z^2$, and T_0 the mean wire temperature. The solution of the second-order differential equation yields

$$T_o(x) = T_o' \exp\left(x\gamma_{1,2}\right) \tag{2.18}$$

$$\gamma_{1,2} = \frac{1}{2D}\left[v \pm \sqrt{v^2 + 4gD^2}\right] \tag{2.19}$$

where γ_1 and γ_2 are for up and downstream the wire, respectively.

Calorimetric flow sensor

The calorimetric flow meter works based on the temperature difference between the two wires. Reading the flow out differentially cancels out noise, like temperature drift, that would otherwise be measured on a single wire.

The temperature distribution of two wires can be found by the superposition of the single wire distributions. Figure 2.4a shows the addition of temperature profiles of two wires. Figure 2.4 shows the changing temperature profile along the channel due to increasing flow, where the difference in temperature over flow velocity is plotted in Figure 2.4c. In the first region (I), the difference in temperature increases reasonably linearly initially

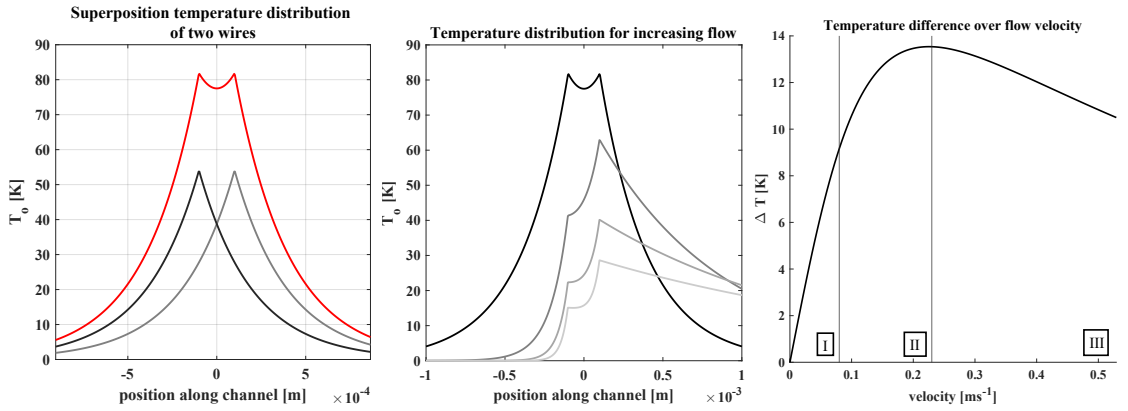

(a) (b) (c)

Figure 2.4: *(a) Moddeled temperature distribution along the channel of two heated wires and, in red, the summation. (b) Changing temperature profile for increasing flow velocities. (c) The temperature difference between the two wires over a flow velocity range.*

due to the downstream heating by the upstream wire's heat plume. The linearity takes off when the flow velocity increases further in (II). When the flow becomes too big (III), the heat boundary layer shrinks, the downstream heating decreases, and both wires start to cool down. Nominal operation of the flow sensor takes place in the first region.

The temperature difference over velocity can be modelled by the superposition of eq. (2.18) separated apart. The difference can be found as

$$\Delta T = T_0 \left[\exp\left(\gamma_1(x - L)\right) - \exp\left(\gamma_1(-x + L)\right)\right] \tag{2.20}$$

with L being the separation distance between the wires.

2.4 Conclusion

In conclusion, this chapter has provided an overview of the fundamental theory of both sensors, focusing on the interactions between paramagnetic gases and magnetic fields, as well as the principles of hot-wire flow sensing.

The interactions of paramagnetic gasses with magnetic fields showed a dependency on temperature and magnetic field gradient. Using the volume force formulas, a model can be made using FEM simulation.

The analysis of heat transfer mechanisms in hot wires, including the impact of fluid flow on temperature distribution, has shown the sensor's dependencies on geometry and flow rate. This will form the theoretical basis for designing, modelling, and optimising the sensor system in the subsequent chapter.

Chapter 3

Design

The paramagnetic effects of oxygen can be measured in several ways. The two phenomena mentioned in Chapter 1 that will be worked out further are the deflection of a gas stream due to the presence of a magnet and thermal-magnetic wind or convection of air. First, a general description of the mechanics of the sensors is discussed. Simulations of the designs will follow this, performed using FEM models of the sensor in COMSOL Multiphysics® 6.2. From the simulations and models, the dimensions extracted are discussed. Lastly, common details shared among the sensors will be covered, including the magnetic field source, sensing wire geometry, and material properties. The design layout masks can be found in Appendix B.

3.1 Deflection sensors

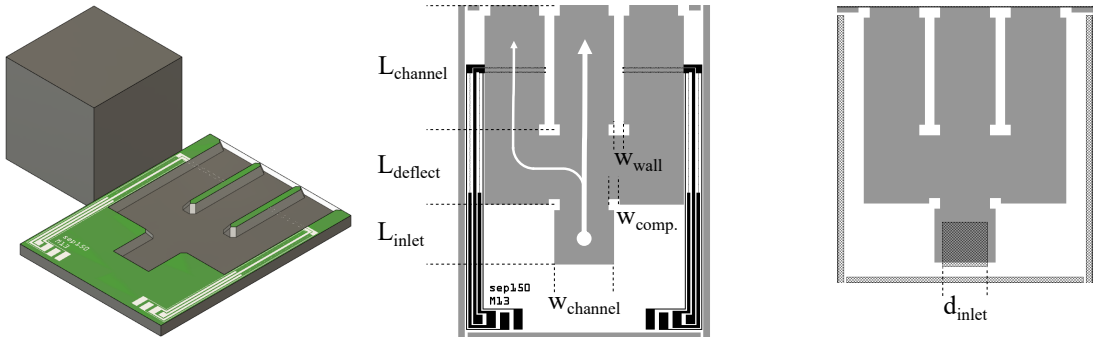

Figure 3.1: *(a) Schematic of the bottom half of the deflection sensor with a 3D representation of the sensor with a* 5 mm *magnet for scale. (b) The layout schematic for the deflection sensor bottom half with dimension parameters. The grey area indicates the channel, and the black area indicates metal. The white arrows indicate the gas flow, and the white dot is the inlet position. (c) The layout schematic of the top half of the deflection sensor. The crossed black area indicates an etch from the other side of the wafer.*

The novel configuration concept of the deflection sensor has been worked out in [7]. The addition of this work is a new and straightforward fabrication method. Instead of bonding a glass wafer to the silicon substrate, two silicon chips will be glued to form channels. The two halves of the channel will be formed using KOH etching, forming a hexagonal duct where the walls will have a slope of 54.74°.

The deflection sensor that is shown in Figure 3.1 works based on diverting part of a gas flow. The sensor consists of an inlet on the bottom, which forks into one middle and side channel, two for symmetry. In the case of no oxygen, the gas stream will mainly flow through the middle. If the gas contains oxygen, part of the middle stream will be attracted

towards the magnet, increasing flow in the side channel. Using a flow sensor, the amount of deflection, which is proportional to the oxygen concentration, can be measured.

FEM simulation

Verification of the working of the sensor concept was done using FEM simulation. The channel geometry was recreated in a 2D simulation. The *Laminar Flow* interface was used to model the gas flow. A fully developed flow rate of $10\,\mathrm{mL\,min^{-1}}$ was set at the inlet, and an atmospheric pressure boundary condition was applied to the outlets at each fork ending. The paramagnetic volume force was modelled using the volume force module with eq. (2.8) with a volume fraction of 21%.

The magnetic B field was modelled using the *Magnetic Fields, No Current* physics interface. The directional components of the magnetic flux density B over the sensor's geometry were fed into the volume force module. The assumption was made that changes created by the magnetisation field of the paramagnetic oxygen are negligible. The remanent flux density of the 5 mm square magnet was set to 1.3 T.

FEM results in Figure 3.2 show similar flow velocities, flow profiles, and flow deflections as were found by Vonderschmidt [7]. Differences could be explained by the exact magnet placement, magnet strength, or the susceptibility value used for oxygen.

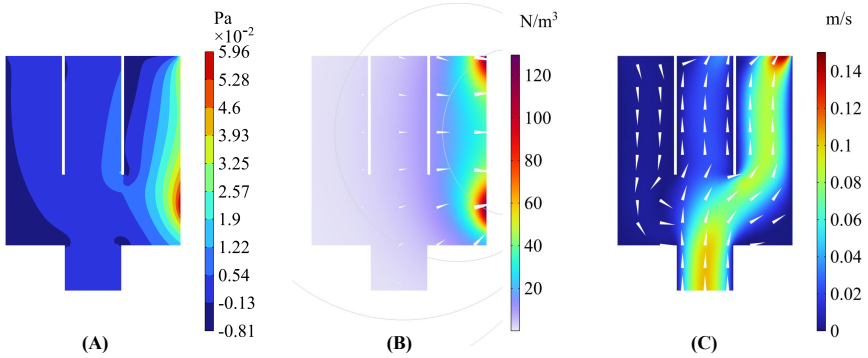

Figure 3.2: *FEM simulation results showing the (A) pressure gradient over the channel, (B) volume force and directional white cones on a logarithmic scale, and (C) the flow velocity distribution and direction with normalised white cones.*

Geometry

The fluid channel geometry has been based on the work done in [7]. The dimensions of the parameters shown in Figure 3.1b can be found in Table 3.1.

The channel width and length for the measurement channel, main channel, and deflection area are chosen based on the optimisation done in the work of [7]. The inlet will form a hole through the chip at the bottom of the fork. The etching will make the narrowest point of the hole roughly a 1 mm square. The channel height has been doubled compared to the sensor by Vonderschmidt to 600 µm. This is taken as an estimated maximum height for two 525 µm wafers that make up the channel to ensure the structural integrity of the channel top and bottom walls and maximize the channel height to reduce the channel flow resistance. The wall width separating the three channels W_{wall} is based on a rough estimation of the expected alignment precision when glueing the two chip halves. Assuming a precision of ± 100 µm this leaves a 230 µm overlap.

Table 3.1: *Dimension parameters of the deflection sensor.*

Parameter	Symbol	Value	Unit
Channel height	$L_{channel}$	4.5	mm
Channel width	$W_{channel}$	2	mm
Channel height	$H_{channel}$	600	µm
Deflection area height	$L_{deflection}$	2.5	mm
Inlet area height	L_{inlet}	2	mm
Inlet dimension	d_{inlet}	1.5	mm
Channel separation walls	W_{wall}	330	µm
Compensation square width	$W_{comp.}$	375	µm
Cleave width	W_{cleave}	210	µm

Compensation structures

The channels will be formed using anisotropic KOH etching to make structures with straight walls. However, under-etching occurs for convex corners in the mask, as the $\langle 110 \rangle$ direction is exposed in the corner. Compensation structures were used to counter this by anticipating the under-etching speed.

A straightforward square structure, as shown in Figure 3.3a, is used as described by Puers in [19]. The compensation structure dimensions are determined with the empirical formula from the paper

$$d = 5.7 + 3.72ed \tag{3.1}$$

with d the relative dimension as indicated in Figure 3.3a, and the etch depth ed, both dimensions in µm. From d, the side of the compensation square, centred at the convex corner, c can be calculated using

$$c = \frac{d \cdot \tan(\alpha)}{\tan(\alpha) + 1} \tag{3.2}$$

where α is approximately 26.6°, the angle between the $\langle 110 \rangle$ and $\langle 130 \rangle$ directions. This yields a compensation structure width c of roughly 370 µm.

Cleave structures

The chips are separated using cleaving, where the wafer is broken along predefined lines. These lines correspond to crystallographic planes in the silicon crystal lattice, which allows the silicon to cleave cleanly. V-grooves are used as starting points for the break to initiate the cleaving process. The v-groove structures are made on both sides of the wafer as shown in Figure 3.3b. The top part needs to be the same depth as the channel depth. At the intersection of v-groove lines a margin W_{stop} was placed to avoid convex corners that can underetch. A test run showed that a remaining cleave thickness T_{cleave} is thick enough to be handled during fabrication while still breakable using slight pressure by hand.

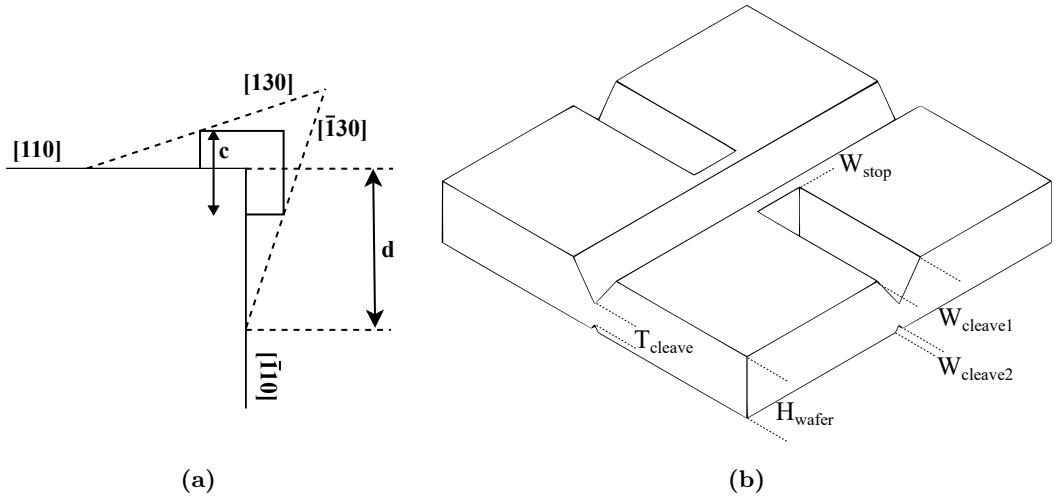

Figure 3.3: *(a) Rectangular compensation structure on an exposed convex corner. (b) Geometric parameters of the cleave structure on both sides of the waver. The bottom side has an identical smaller v-groove pattern.*

Table 3.2: *Dimension parameters cleave structure.*

Parameter	Symbol	Value [µm]
Cleave width top mask	W_{cleave1}	420
Cleave width bottom mask	W_{cleave2}	70
Remaining cleave thickness	T_{cleave}	175
Cleave cross margin	W_{stop}	100
Wafer height	H_{wafer}	525

3.2 Magnetic Wind Sensor

The magnetic wind sensor works based on the temperature dependency of the susceptibility of oxygen (eq. (2.1)). Air is fed into the sensor from the bottom, as indicated by the white circle in Figure 3.4, which symmetrically connects the two side channels. Cool oxygen will be attracted to the magnet from both side channels. Under the right side of the magnet in the channel, a heater will increase the temperature of the gas, decreasing its susceptibility. The asymmetry in temperature causes a net force towards the right, referred to as thermomagnetic convection or wind, which a flow sensor can measure. As both side channels receive an equal flow rate, the pressure difference across the sensing channel through the middle of the sensor should not experience any flow if no heat or oxygen is present.

FEM simulation

A 3D COMSOL model is made using the same *Laminar Flow* and *Magnetic Fields, No Current* interface settings as for the 2D deflection sensor model. Additionally, the *Heat Transfer in Solids and Fluids* interface is used to model the temperature distribution around the heater. The heater in the middle of the plane is modelled as a 2D surface. The temperature distribution is then fed to the volume force to approximate the total susceptibility as described in eq. (2.2).

The flow inlet is set as a fully developed flow rate boundary condition at $10\,\text{mL}\,\text{min}^{-1}$.

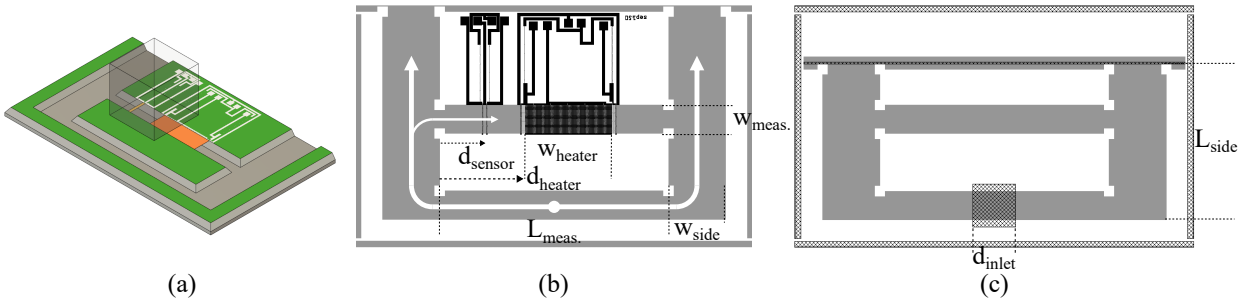

Figure 3.4: *(a) Schematic of the magnetic wind sensor with the magnet as a transparent cube above the top half of the chip, which is not illustrated. The yellow and orange surfaces across the channel indicate the sensor and heater, respectively. (b) The layout schematic of the magnetic wind sensor. The grey area indicates the channel formation, and the black area indicates the metal layer. The white arrows indicate the flow direction, and the white dot indicates the inlet point. (c) The layout of the top half of the magnetic wind sensor where the crossed black area indicates the etch from the other side of the wafer. The top part of the chip will be cleaved off.*

Table 3.3: *Dimension parameters magnetic wind sensor.*

Parameter	Symbol	Value [mm]
Width measurement channel	$W_{meas.}$	1
Length measurement channel	$L_{meas.}$	8
Distance sensor from the side	d_{sensor}	1.55
Distance heater from the side	d_{heater}	3
Width heater	W_{heater}	3
Width side channel	W_{side}	2
Length side channel	L_{side}	5.5
Inlet dimension	d_{inlet}	1.5

The sensor's side channels are connected to a larger air volume, and on the other side, an atmospheric pressure boundary condition is set. A temperature boundary condition is set on the outside of the 2D sensor at 20 °C and on the heater at 120 °C. For the magnetic field, a 3 mm magnet is used with a 1.3 remanent flux density.

Figure 3.5 shows the resulting temperature and velocity plots for the magnetic wind sensor. A 1D view from the middle along the measurement channel is shown in Figure 3.6b for two magnet positions. The black line shows the volume force along the measurement channel distance in the case of no heater, the red line shows the volume force with heater, and the grey line shows the temperature along the channel. In the case when the magnet is left of the heater, indicated by the solid red and black lines, the volume force under the heater is lower compared to no heater. The same, but in the opposite direction, is visible for the dotted lines when the magnet is on the right side of the heater.

The resulting flow from the asymmetric volume force is shown in Figure 3.6b. The positive flow direction is from left to right in the sensor's top-down view. A positive magnet position relative to the heater is towards the left of the heater. The simulation shows a change in flow direction when the centre of the magnet crosses the centre of the heater. An optimum velocity in the positive direction can be seen for a relative position of 1.5 mm or half a magnet width. The flow in the measurement channel with and without a heater seems to have an offset. In the case of no heater, a fairly consistent flow independent of magnet position is observed around 1.8 $\mathrm{m\,s^{-1}}$. In the case with a heater, a similar offset

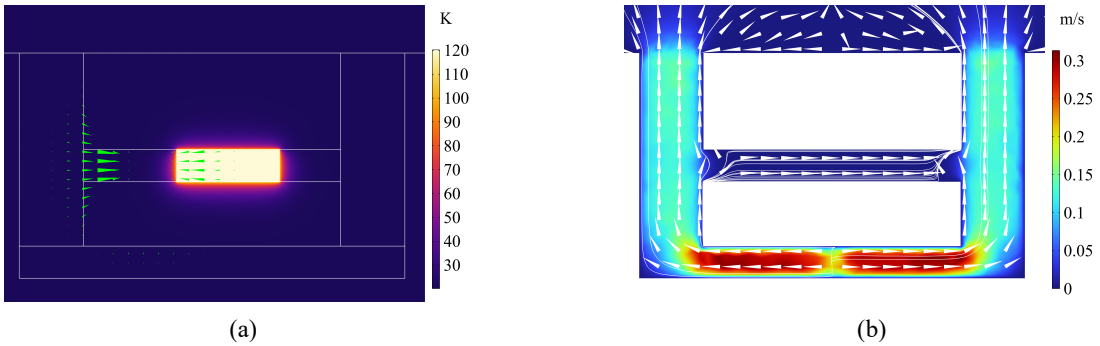

Figure 3.5: *(a) 2D plot of the temperature distribution, with the white outlines indicating the channel shape, and the green cones showing the volume force direction and magnitude scaled linearly. (b) A 2D velocity magnitude profile with the white cones indicates the flow direction.*

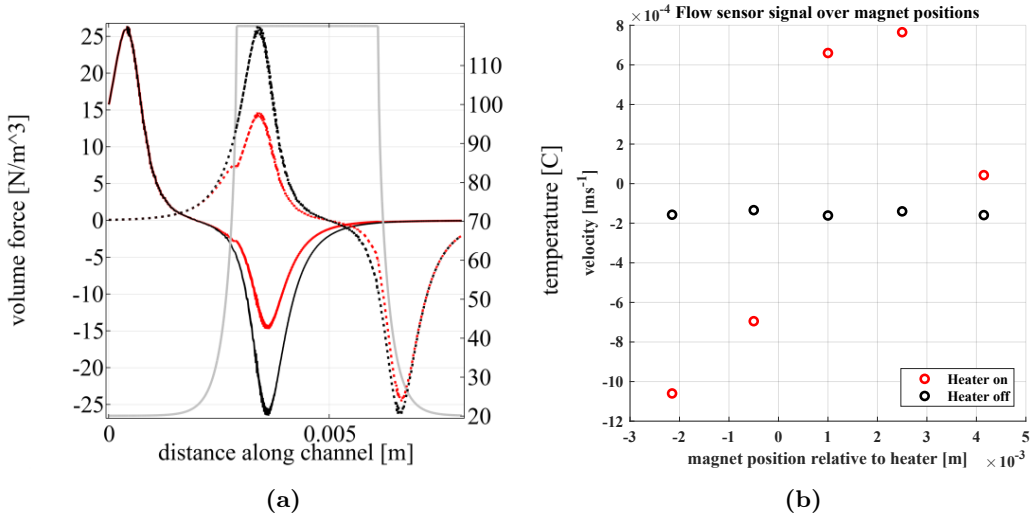

Figure 3.6: *(a) The volume force at the centre of the measurement channel for, in red, with heater, and in black, without heater. The two positions are indicated by the solid line, 0.5 mm downstream, and the dotted line, 2.5 mm, with respect to the centre of the heater. The grey line shows the temperature distribution. (b) The average flow velocity in the channel for a range of magnet positions.*

for an interpolation between the two points is shown where the relative magnet position is 0. This could be the result of a meshing issue, causing slight asymmetries in flow leading to a flow in the measurement channel.

Geometry

The dimensions of the magnetic wind sensor are listed in Table 3.3. Making the measurement channel narrow helps to reduce the influx of air passing from the side channels. However, the flow sensor's length to cross-sectional area ratio worsens for a narrower channel, leaking relatively more heat to the substrate. The middle ground was chosen roughly at 1 mm. The length of the measurement channel needs to fit a magnet and heater. A magnet of 3 mm is chosen based on its reach and volume force for a channel height of 600 µm, which is further explained in Section 3.2. To create the largest asymmetry in volume force, the heater is only placed from the middle towards the right of the magnet.

The wider the heater, the larger the range over which the volume force will be reduced. Therefore, a conservative width of 3 mm was chosen for the heater. The length of the measurement channel was set at 8 mm to make room for both the flow sensor and heater.

3.3 Magnetic field source

For these sensors to have the most effect, both the volume force magnitude and the range of influence should be optimized. Neodymium permanent magnets are chosen for their large magnetic field of around 1 to 1.3 T. This field magnitude does not increase with volume but is a material property of ferromagnetic materials, which is the magnetization alignment retained after exposure to an external magnetic field.

Magnetic fields induced by coils are generally weaker than those produced by permanent magnets. For the purposes of these MEMS sensors, achieving a field strength comparable to neodymium magnets would require large currents through small coils. This approach would introduce significant heating issues, making it less practical.

The volume of neodymium magnets influences the shape of the field lines, affecting the volume force magnitude. This force is proportional to the gradient of the squared magnetic field. A larger magnet volume produces field lines that extend further but with a decreased gradient, potentially reducing the volume force at certain distances.

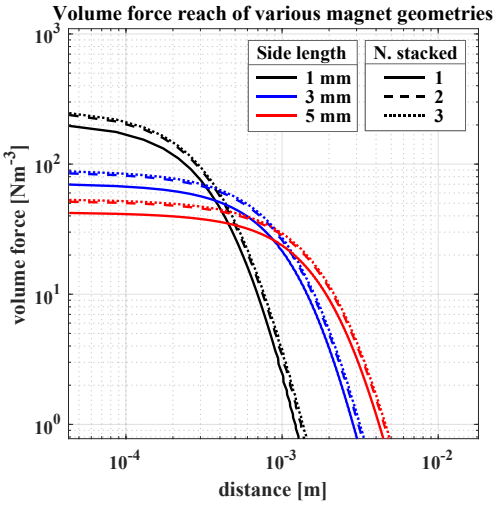

Figure 3.7: *Volume force magnitudes over distance for various common cubic magnet sizes for a remanent flux density of* 1 T. *Also the distribution is shown for additional stacked magnets.*

Figure 3.7 shows a FEM simulation of various magnet sizes and their corresponding volume force distributions. The optimal magnet size is chosen based on the required MEMS sensor reach, aiming to maximize the volume force within the sensor's operational range. For the deflection sensor, a 5 mm cubic magnet is chosen to have a roughly 1 mm distance reach to deflect the gas stream from the inlet. A 3 mm magnet is used for the magnetic wind sensor to ensure enough range centralised over the heater. The minimal distance over which the magnet needs to exert a volume force is determined by the thickness of the wall between the magnet and the channel. This is set to 200 µm.

3.4 Flow sensors

Changes in flow will be measured with the calorimetric sensor as described in Chapter 2. The up and downstream resistors will be part of the bottom half of a Wheatstone bridge configuration, allowing for the differential change in resistance to be read out.

The geometry of the calorimetric flow sensor determines the sensitivity and the operational flow range. The FEM simulations for the deflection sensor show a range from 0 to 0.1 $\mathrm{m\,s^{-1}}$, whilst the magnetic wind sensor shows a range of 0 to 1 $\mathrm{mm\,s^{-1}}$. The optimal geometry was found using Lammerink's model and sweeping over the wire separation distance, the channel width L_y, and half the channel height L_z.

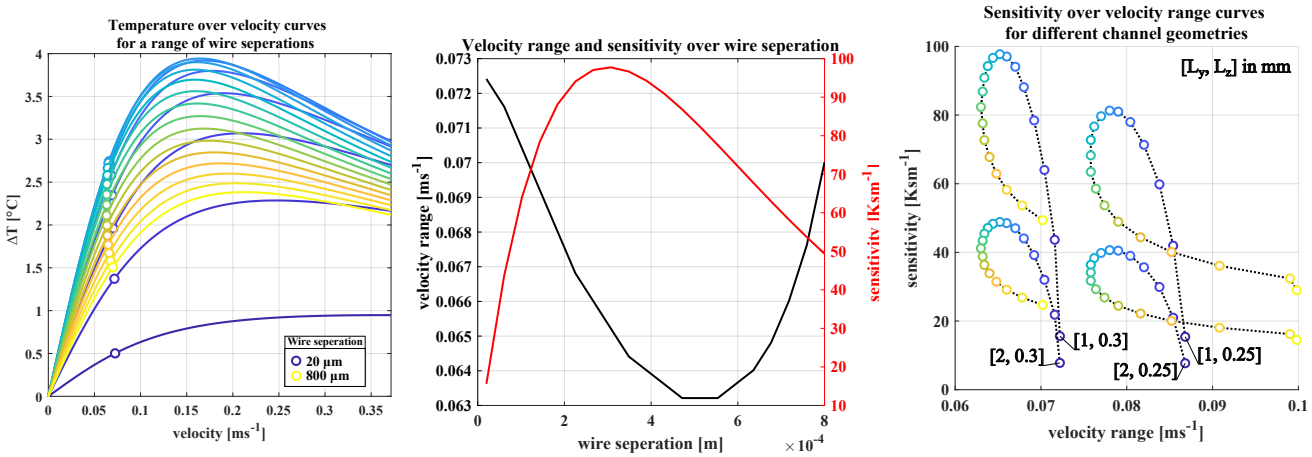

(a) (b) (c)

Figure 3.8: *(a) Temperature difference against flow velocity or air for a range of wire separation distances for a channel width of* 1 mm *and the markers showing the velocity range. (b) Velocity range and sensitivity over wire separation distances. (c) sensitivity over velocity range curves for a range of wire separation distances and combinations of channel widths L_y and heights L_z.*

Figure 3.8a shows the temperature difference between the calorimetric wires ΔT for increasing flow velocity curves for a span of wire separation distances. The flow range, indicated by the markers, is the linear operating range of the sensor. The upper operating point is taken at the maximum of the ΔT velocity curve's second derivative. Figure 3.8b shows an inverted trend for the range and sensitivity, where the sensitivity is taken as the maximum value of the first derivative of the ΔT over velocity curve. Figure 3.8c plots the sensitivity over velocity range for a range of wire separations and various channel geometries. It shows similar loops for sweeping over wire separations. A wider and higher channel increases the sensitivity. A higher channel also reduces the velocity range.

The increasing sensitivity for narrow channels results from increasing wire temperature due to less conduction through the fluid to the channel walls. This will be limited as the increasing width-length ratio increases the significance of the heat leakage to the substrate. Expanding the channel height increases the downstream heat from the upstream wire, effectively increasing the wire temperature but reducing the range for the same wire separation.

The channel widths of the sensors are approximately set by observing the flow behaviour with FEM simulations. The height is maximised to lower the channel resistance and to have a shorter distance from the magnet. The separation was chosen based on the highest sensitivity for the required range and channel dimensions. This yields a wire separation of 270 µm and 150 µm for the deflection and magnetic wind sensor, respectively. A few extra

sensors were made for calorimetric sensor characterisation using deviating wire separations of 80 µm and 300 µm for the magnetic wind sensor, and 160 µm for the deflection sensor.

Geometry and materials

The signal the wires produce as a change in resistance is proportional to the temperature as $\Delta R = R_a \alpha \Delta T$. A larger resistance at ambient temperature R_a would increase the changes in resistance measured for the same temperature difference. Increasing the wire's resistance can be done by increasing the length to crossectional area ratio. Whilst decreasing the crossectional area increases the resistance, it decreases the current that can be applied due to electron migration. This sets a maximum on the current density that has been found to be around 10^{10} A/m^2 for platinum [12] [20].

Platinum is chosen for the wire for its relatively high-temperature coefficient α, high mean time to failure (MTTF) for electron migration [20], and high melting point. Additionally, platinum is fabricated easily in thin layers and resistant to KOH etching. An 100 nm film thickness is chosen with a width of 1 µm; limited by the litography resolution.

Bridging the channels, a silicon-rich silicon nitride (SiRN) film is chosen as it is resistant to the etching steps. The stresses in the film layer are reduced due to the increased silicon concentration compared to stoichiometric silicon nitride, improving the stability of the wires. A thickness of 500 nm has been chosen as a film thickness for reliable fabrication whilst keeping the heat losses to the substrate low. As platinum does not adhere directly to untreated SiRN, an adhesion layer of 10 nm chromium is used. Even though studies have shown chromium being etched by KOH, tests have shown that it still holds as an adhesion layer between platinum and SiRN [21].

For deflection and magnetic wind sensors, wires cross a channel and arrive at a disconnected island, requiring them to loop back. The wire loop is designed to be narrow compared to the length and separation of the calorimetric wires. The structure is then approximated as a single wire over the channel with an effective doubled resistance. A problem that can occur by placing narrow free-hanging wires close to each other is that capillary forces during wet steps in the process can cause them to tangle up or break. Figure 3.9 shows the devised mesh-like structure in the SiRN layer as a carrier for the wires to have a mechanical connection. To avoid the wire mesh obstructing the KOH etching of the channel, diagonal lines are used so that the under etch will meet under the bridge. This prevents the etching from coming to a halt due to the $\langle 111 \rangle$ plane.

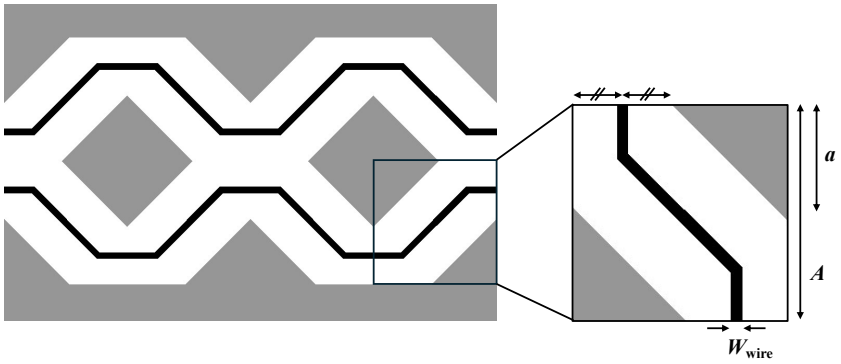

Figure 3.9: *Diagram of the wire structure with in white the SiRN film, black the metal layers, and grey the channel underneath.*

The SiRN mesh dimension restrictions for the geometry shown in Figure 3.9 can be

calculated using the under-etching speed with

$$\frac{1}{2}A - a > d \tag{3.3}$$

where A is the mesh element size, a is the hole size, and d is the under-etching distance parallel to the $\langle 100 \rangle$ plane in the $\langle 110 \rangle$ direction.

The same mesh structure forms the heater for the magnetic wind sensor. For the sensing wires and heater, A was set to 20 µm with an a/A ratio of 0.5. A test run of the mesh geometry dimensions is included in Figure B.3. For the heater W_{wire} was set to 7 µm.

3.5 Macro connections

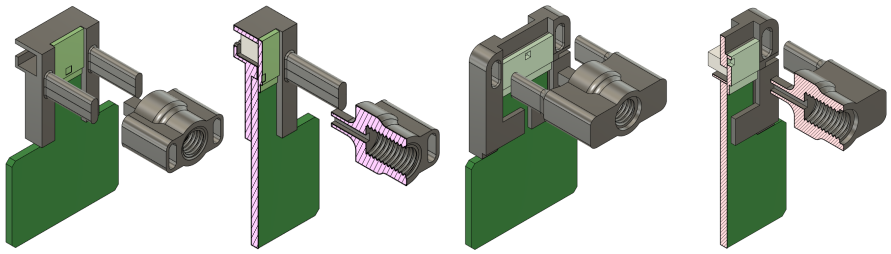

Figure 3.10: *Two variations on the 3D printed mounts on the breakout PCB with (a) the deflection sensor and (b) magnetic wind sensor designs.*

Electrical connections to the chip are made with aluminium wire bonds to a breakout PCB. To align the sensor to the PCB, a mount was designed that also serves as a gas adapter, as shown in Figure 3.10. Two pins guide the gas adapter to align with the through chip inlet hole on the sensor and provide support by deflecting mechanical stresses via the mount to the PCB rather than directly on the chip. The printed threads allow a connection with a 1/4-28 standard flat-bottom port plug. Both mounts have a slot to hold the magnet while allowing for adjustments in the horizontal position.

3.6 Conclusion

This chapter has presented the design and simulation of two oxygen sensors based on the paramagnetic properties of oxygen: a deflection sensor and a magnetic wind sensor. Both sensors utilize the interaction between oxygen and magnetic fields to detect and measure oxygen concentration in gas streams. The designs have been analyzed using FEM simulations in COMSOL Multiphysics, verifying the working principles.

The fabrication method proposed for these sensors involves an approach of gluing two silicon chips to form channels, with KOH etching used to create the channel structures. The geometry of the sensors, including channel dimensions, compensation structures for etching, and cleaving structures for chip separation, have been covered. The magnetic field source for both sensors with neodymium permanent magnets was selected based on the volume force and reach. Flow measurement in both sensors is achieved through calorimetric flow sensors, which have been designed and optimized for each specific application. Material selection is also a critical aspect of the design, with platinum wires on a silicon-rich nitride film chosen for their suitable properties and compatibility with the fabrication process.

Chapter 4

Fabrication

This chapter will discuss the fabrication process in more detail. It will describe the cleanroom fabrication flow covering the wafer alignment, lift-off metal, and anisotropic etching. Lastly, the sensor assembly will be shown.

4.1 Fabrication process

The three sensors' bottom and top half are fabricated using a single 100 mm Double Side Polish (DSP) wafer 525 ± 10 µm thick. Photomasks and the full process flow with instrument parameters, and some preliminary etching tests are included in appendix B.

⟨110⟩ aligning

Due to the highly directional KOH etching, the wafer must first be aligned with the ⟨110⟩ directions. Using symmetric Vangbo patterns, the subsequent masks can be aligned with an approximate 0.05 degree of accuracy compared to the 1 degree of accuracy the wafer flat provides [21][22]. The Vangbo mask is prepared using a hard mask compatible with the KOH etchant. The process begins by depositing a 100 nm layer of low-pressure chemical vapour deposition (LPCVD) SiRN on the wafer. Next, a photoresist layer containing the Vangbo patterns is developed, and reactive ion etching (RIE) is used to etch the SiRN. After removing the carbonized photoresist from the wafer using oxygen plasma etching, the wafer is etched in HF for 3 min to remove any oxidation that could interfere with the KOH etching. This is followed by the anisotropic etch in a 75% by weight KOH solution at 75 °C for 15 min. The resulting patterns are shown in Figure 4.1.

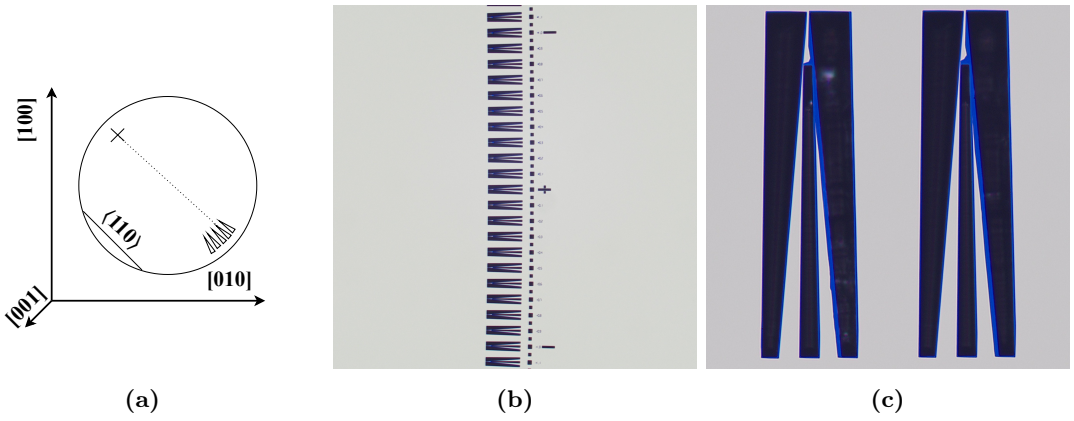

Figure 4.1: *(a) A schematic depiction of the Vangbo mask on the wafer with the silicon crystal orientations. (b) The semicircular array of structures (c) Zoomed-in set of asymmetric Vangbo forks where the right prong is over-etched. Black shows the etched parts, and blue shows the hanging SiRN layer. The fork is roughly* 340 µm *by* 95 µm.

The narrow prongs of the fork allow for visually noticeable changes in symmetry due to the etching speed change with angle. Aligning a dot on one side of the wafer with the symmetric prong position on the other side results in a line parallel to the ⟨111⟩ planes.

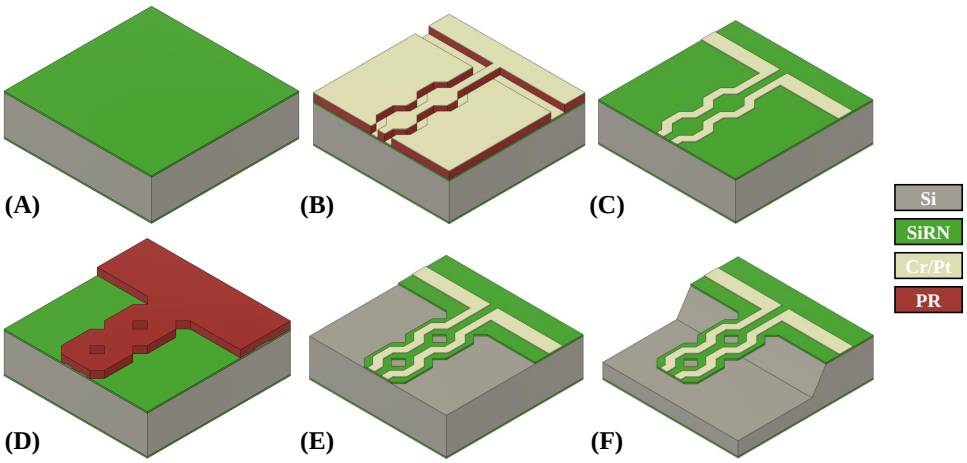

Figure 4.2: *Processflow overview for a wire over a channel. (A) LPCVD SiRN on Si, (B) photoresist deposition and exposure with evaporated metal on top, (C) lift-off, (D) hard mask patterning, (E) RIE SiRN, (F) KOH etching.*

The processflow is schematically depicted in Figure 4.2. The process is continued by replacing the Vangbo hardmask with a 500 nm SiRN layer (Figure 4.2A).

Liftoff metal

The metal pattern is applied using a lift-off method (Figure 4.2B). For this *AZ 3001* photoresist was used to achieve steep resist-sidewalls. On top of the photoresist a 10 nm and 100 nm Cr Pt layers were evaporated respectively. This allowed for a highly directional application of metal. Subsequently, the resist was removed in an ultrasound bath submerged in acetone at room temperature (Figure 4.2C).

SiRN etch windows

The SiRN is again used as a hard mask for the KOH etch using the same procedure as was used for the Vangbo mask. The same procedure was performed on the backside of the wafer. Openings in the hard mask were made using ion beam etching (IBE) (Figure 4.2E). However, this could have been done using RIE for the fabrication of the structures shown.

KOH etching

Etching was performed with a 5-hour etch with 25% KOH at 75 °C. An etching speed was found of 1.07 µm min^{-1} for the ⟨100⟩ plane. For underetching parallel to the ⟨100⟩ plane in the ⟨111⟩ direction a speed was found of 18 nm min^{-1}, and for the ⟨110⟩ 1.3 µm min^{-1}.

The resulting fabricated chips are shown in Figure 4.3 following the designs of Figure 3.1 and Figure 3.4.

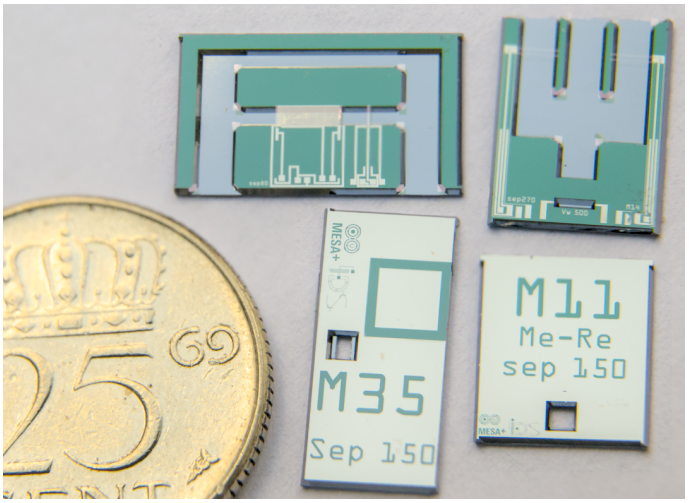

Figure 4.3: *The fabricated sensors with on the top the channels with the sensing structures and on the bottom the covers, containing the other half of the channel and inlets. The magnetic wind sensor is shown on the left, and the deflection sensor on the right.*

4.2 Sensor assembly

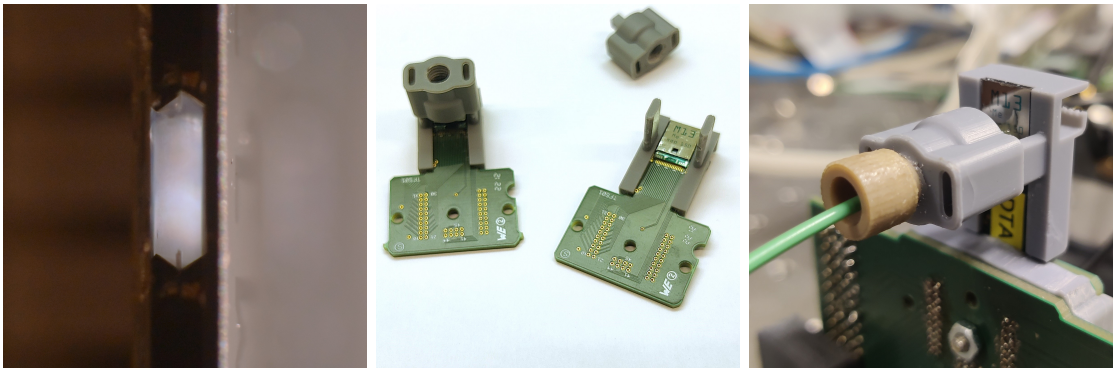

(a) **(b)** **(c)**

Figure 4.4: *(a) Hexagonal channel of the deflection sensor where the middle channel is lit from behind via the inlet. (b) Chip stack electrical and gas connections. (c) The chip gas adapter.*

The sensors consisted of two silicon chips, the bottom half formed the lower half of the hexagonal channel and contained the metal layer with the resistive sensors and heaters, and the top chip formed the other half of the channel and contained the inlet through-chip hole.

With KOH etching, v-grooves were formed on both sides as cleaving guides to separate the chips from the wafer. Once cleaved, the chip halves were glued together using low viscosity *LOCTITE 4305 LC* UV-glue. Using a resin-printed jig with a square alignment corner, the chip stack was glued only from the sides. An approximate alignment deviation of 30 µm could be achieved. Figure 4.4a shows an example of two bonded chip halves. The chip stack was bonded to a breakout PCB using a two-part epoxy. Electrical connections to the PCB were made using aluminium wire bonds (Figure 4.4b). Feeding in the gas mixture was done using a custom 3D-printed mount(Figure 4.4c) as described in Section 3.5. The gas connection between the chip and adapter was sealed with epoxy.

4.3 Results and discussion

Liftoff metal

Some ear formation was visible on the lift-off metal due to the metal covering of the resist-sidewall. This resulted in metal parts getting stuck in the dense metal mesh. However, most ear formation vanished after the KOH etch step.

Ear formation could be mitigated by using a secondary layer that can be under-etched from the developed photoresist. Spin on LOR can be used as an underlayer, and a standard photoresist can be developed on top. By adjusting the baking time of the sacrificial layer, the etching speed can be adjusted. Once the photoresist is developed, the developer will under-etch the LOR layer underneath, creating large overhang structures, effectively a negative resist-sidewall taper.

A more accurate method of etching the metal layer with the SiRN bridge in one step could be done by creating wide metal traces and using IBE together with the SiRN in step E in Figure 4.2 as has been done in [21]. The self-aligned step avoids margins needed for alignment and allows narrower widths for the SiRN bridge. Sensor variations using wires directly formed using this self-aligned step for the wires above the channel showed narrower wires than the wires made on a plane of SiRN. Signs of flaking of the metal layer were also observed.

Flaking could result from several steps. The ears of the liftoff procedure might have acted as leverage points for the flakes to become loose. Another reason might be the chromium layer being etched during the KOH step, loosening the platinum layer.

KOH etching

A fabrication test run of the compensation structures (Figure B.2) showed under etching beyond the designed convex corner. As the channel shapes were not necessarily designed to have perfectly straight corners, the compensation square dimensions were retained in the final design.

4.4 Conclusion

In this chapter, the fabrication process for the sensor components was discussed, highlighting steps involved in wafer alignment, metal liftoff, and anisotropic etching using KOH. The integration and assembly of the sensor components were covered. The discussion section addressed challenges encountered during fabrication, such as ear formation in the liftoff metal and under-etching during KOH etching, and provided potential solutions to these issues.

Chapter 5

Measurement methods

5.1 Measurement setup

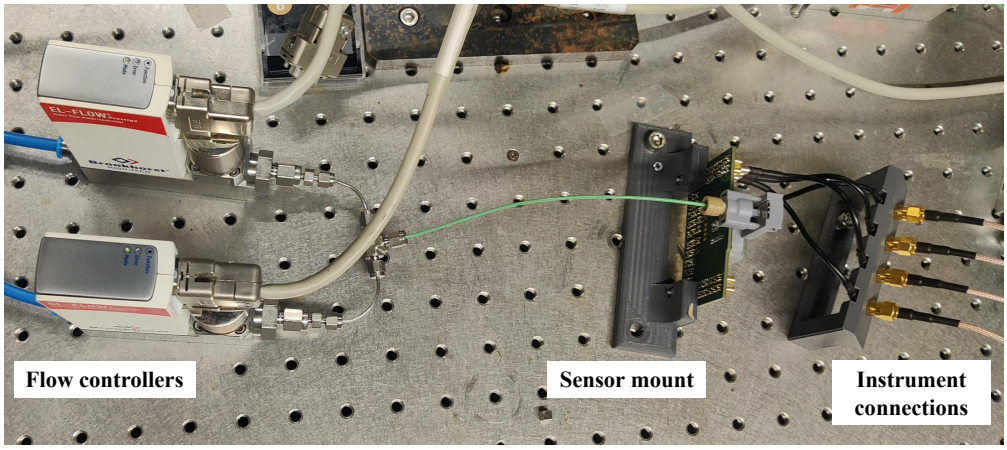

Figure 5.1: *Photo of the measurement setup.*

Figure 5.1 shows the measurement setup used to characterise the sensors. The assembled deflection and magnetic wind sensor are both compatible to be bolted onto the sensor mount. A plastic bag was put over the sensor for each measurement to avoid interference from external flow sources.

Voltage measurements were taken using the *Keithley 2000* multimeter with an integration of 1 NPLC and auto-range enabled. An *Keithley 6487* was used as a power source for the Wheatstone bridge. The heater in the magnetic wind sensor was powered by a constant current from a *Keithley 6221* current source.

The gas composition was controlled using the Bronkhorst flow controllers *EL-FLOW Prestige FG-201CV*. Compressed air and N_2 were fed into 8 and 10 $\mathrm{mL\,min^{-1}}$ flow range flow controllers, respectively. The oxygen volume percentage of the output mixture can be determined by mixing the controlled gas outlet flows of the two controllers while maintaining a constant flow rate. Knowing the volume rate fraction to the total flow rate, the oxygen concentration can be calculated assuming a 21% oxygen concentration in air.

5.2 Measurement methods

Burn-in

One reason for signal drift is changes in the metal traces at elevated temperatures. Due to the cold deposition layer, stresses can build up in the film, accompanied by lower densities and grain sizes [23]. Heating the wire can alter these properties, leading to, among other

factors, changes reflected in the measurements.
Two general solutions are found for this. First, the chip is annealed at temperatures higher than the operating temperature. There is not a single procedure for this problem due to the many factors that can lead to this temperature-dependent drift. An anneal of 300 for 5 h in ambient air reduced resistivity roughly with 5%. Higher temperatures would likely address a more extensive range of drift-causing factors, but a capping layer on the metal is needed to prevent oxidation.
The second and also applied option is to anneal the wire by joule heating. The current density limits the temperature range for the sensors in this work to between 100 and 150 °C. A burn-in time of 30 min at 1.5 $\mathrm{A\,m^{-2}}$ was performed once for each sensor.

Magnets

A 3 mm (N45 [24]) and 5 mm (N50) cubic magnet was used for the deflection and magnetic wind sensor respectively. Both were held on the sensor with a resin-printed mount. During measurements, magnets were held stationary to prevent induced voltages in the traces. After placing the magnet the system was allowed to equalise in temperature as the thermal mass of the magnet could transmit enough heat to be visible in the signal of the flow sensors.

Flow rate measurements

Anemometer measurements used a four-point measurement with a constant current while reading the voltage drop over the resistive element. Two flow controllers of 10 and 100 $\mathrm{mL\,min^{-1}}$ N_2 are connected in parallel to provide a wider flow rate range. The corresponding velocity is found by dividing the flow rate by the hexagonal crossectional area. Velocity measurements alternated between increasing steps with zero flow to eliminate drift. The zero flow measurements are then used to measure the drift with a zero flow voltage value at the start of the measurement. Fitting the flow rate behaviour is done using the hot wire model of Bruun (eq. (2.12)) by fitting the heat transfer coefficient parameters.

Oxygen measurement

The oxygen sensitivity is measured as the voltage change per percentage of oxygen change in the inlet gas. To confirm the sensor's selectivity to the oxygen percentage, the same tests are performed using no magnet, nitrogen instead of air, and no heater in the magnetic wind sensor case. As the slope of voltage per oxygen percentage with a magnet also contains the sensitivity to flow rate changes, the measurements without a magnet can be used as a reference point. Subtracting the slope of the oxygen sensitivity in the case of no magnet is used to exclude the flow rate sensitivity.

The oxygen sensitivity slope is measured using incrementally increasing air fraction of the total inlet flow of $10\,\mathrm{mL\,min^{-1}}$. Increments of 10% from 20% to 80% where hold for 30 s. For each change in flow rate a rest period of 10 s was used and for each wire temperature change 180 s. The sample rate of the multimeter was around 4 Hz.

Chapter 6

Results and discussion

This chapter presents the experimental results, followed by a discussion of the different flow sensor designs explored in this work. The chapter is divided into several sections, each focusing on a specific part of the sensors and their characterization. The first section covers the characterization of the flow sensor used for the deflection sensor with a channel width of 2 mm and the magnetic wind sensor with a channel width of 1mm. This will begin with the temperature coefficient of the metal wires used in the flow sensors, which will provide information about the thermal properties of the sensing elements. The flow characteristics with single and dual heated wire operation will follow. After the flow sensor measurements, the paramagnetic sensor results are analyzed and compared to the FEM models.

6.1 Flow meters

Temperature coefficient

Figure 6.1 shows the four-point measurement of the resistance over temperature measurements of two wires, $38.4\,\Omega$ and $95.6\,\Omega$ for R_1 and R_2 respectively. Measurements were performed by changing the temperature in an oven in both directions. The fits both show an $R^2 > 0.999$ and have a combined average temperature coefficient α of $0.0017\,K^{-1}$. No significant hysteresis is observed.

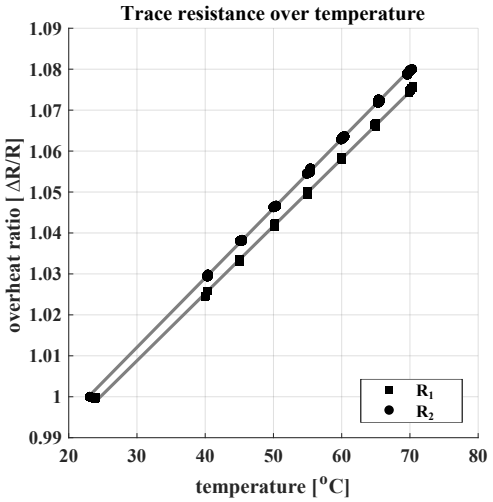

Figure 6.1: *The change in resistance over temperature. The measurements have been normalised by their overheat ratio, where the change in resistance is divided by the resistance measured at room temperature.*

The temperature coefficient value is less than half the value for bulk platinum of

$0.0039\,\mathrm{K}^{-1}$ [25]. The temperature coefficient, however, does fit the value found in [26] for 100 nm platinum of approximately $0.0018\,\mathrm{K}^{-1}$.

Anemometer

The anemometer temperature over flow velocity measurements are shown in Figure 6.2 with the resulting fitting parameters in Table 6.1 using the model described in Section 2.3.

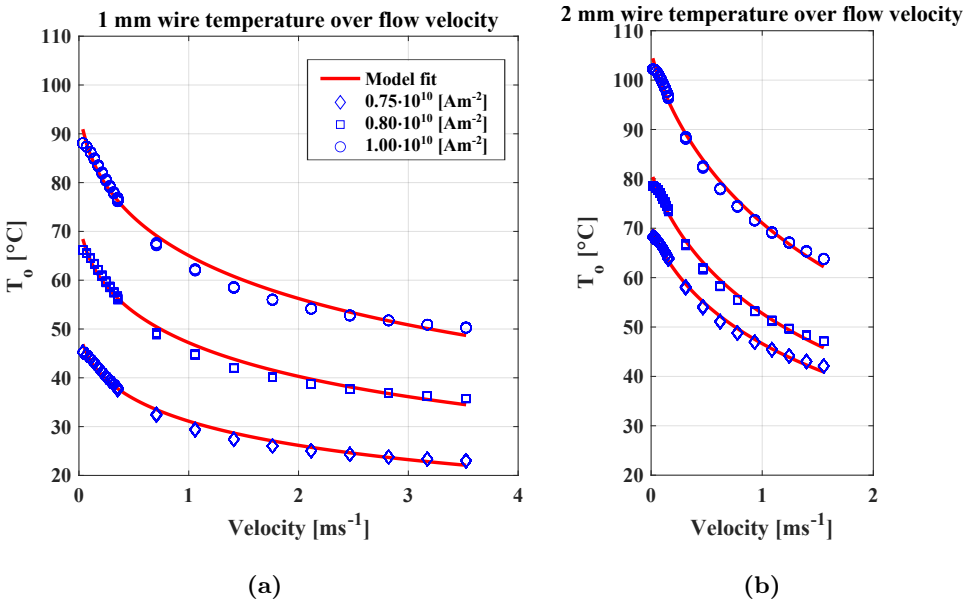

(a) (b)

Figure 6.2: *Temperature against flow velocity of (a) 1 and (b) 2* mm *channel widths.*

Table 6.1: *Fitting parameters from Figure 6.2.*

	1 mm			2 mm		
current density $[\mathrm{A\,m^{-2}}]$	A	B	n	A	B	n
0.75	82.83	67.53	1.75	54.66	38.71	1.28
0.80	62.59	46.53	1.79	55.56	40.13	1.23
1.00	85.18	48.83	1.8	78.16	43.57	1.22
mean	76.87	54.30	1.78	62.79	40.80	1.24

The individual model fits result in an $\mathrm{R}^2 > 0.99$. However, all fits show a difference in curvature compared to the data. The thermal transport coefficient h is larger than expected. In the case of no forced flow, A, representing free convection, is 3 to 4 times larger than textbook values [14]. The value of n also shows an inconsistency between wire lengths, showing a lower value for a longer wire.

The discrepancy in heat transfer coefficient could be due to missing heat loss components in the model or geometry related deviations. The model neglects the conductive losses through the fluid to the channel walls. The fluid conductance could make the thermal conduction coefficient larger if it also encapsulates its heat losses. This significant factor is also flow-dependent; the thermal boundary decreases with increasing flow. Hence, there is a change in both conduction and convection terms A and B with the wire temperature, or power, and flow velocity.

A minor contribution to the deviation could be the model's assumption that h is constant over the wire when, in reality, it changes along the wire due to the proximity changes to the channel walls and the fluid velocity boundary.

However, sources have reported similar higher than expected h values for narrow beams with the same method [27] [28].

The deviation in exponent n from nominal anemometer values of 2, and changes between wire lengths, could be related to the change in geometry. Values between 1.3 to 1.7 have been reported by [29] for similar micromachined anemometers. Deviation from $n = 2$ has also been observed for anemometer operation type: constant temperature or constant current [17].

Calorimetric

The voltage output measurement of the sensors is shown in Figure 6.3 for both the 1 and 2 mm channel widths. The extracted sensitivity and range are plotted in Figure 6.4.

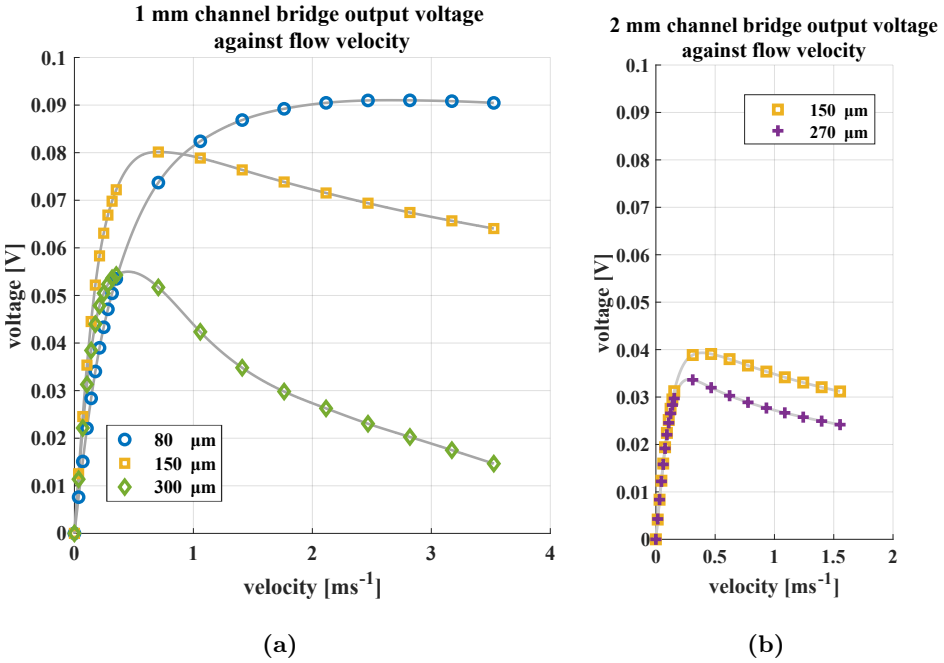

Figure 6.3: *Voltage against flow velocity of (a) 1 and (b) 2* mm *channel widths. With the markers showing the various beam separation configurations and the gray line indicating a spline fit trend. All lines were taken at the same current density of* $1\,\mathrm{A}^2\,\mathrm{m}^{-1}$.

Looking at the extracted sensitivities for different sensor geometries in Figure 6.4, the largest value is found for the 150 µm wire separation for the 1 mm channel width. Deviating from the 150 µm wire separation shows a decrease in sensitivity. Also visible is a lower sensitivity for increased channel width and a decrease in velocity range for wider wire separations.

Comparing the values with the model shows that the measured velocity range is more than twice as large. Overall the trends of sensitivity and range with channel width and wire separation are coherent with the model. However, there are too few data points to verify the trends.

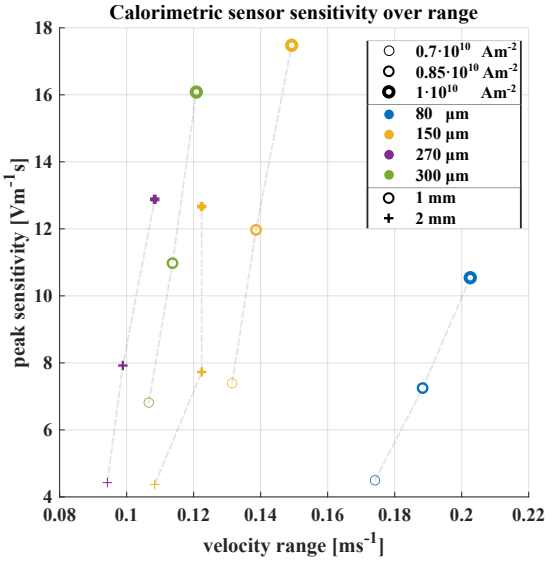

Figure 6.4: *The peak sensitivity against velocity range of calorimetric flow sensors. Various beam separations are indicated by the marker colour, the marker symbol indicates the channel width, and the marker linewidth shows the current density applied. The grey dotted lines connect the measurements for a single device.*

6.2 Deflection flow sensor

Figure 6.5 shows the output voltage of the Wheatstone bridge as a function of the flow rate ratio of the flow controllers.

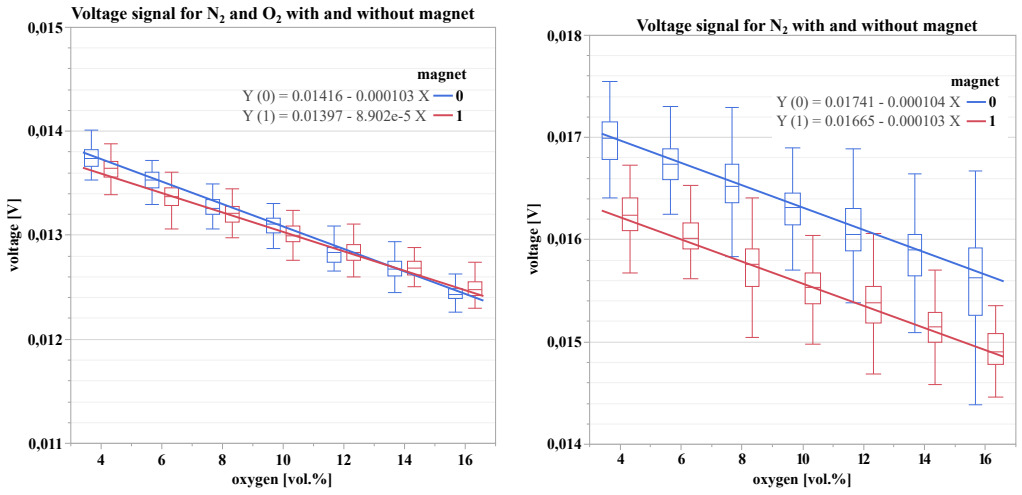

(a) (b)

Figure 6.5: *Boxplots and the trend in voltage over a change in flow rate ratio of two flow controllers. The red and blue colours show the presence and absence of a magnet, respectively. The x-axis represents the volume fraction of oxygen. Figure (a) shows the results obtained when oxygen gas was used, while Figure (b) shows the results obtained when only nitrogen gas was used. Despite the difference in gas composition, the x-axis scale is the same for both figures, as it represents the volume fraction that would have been present if air had been used in both cases. The equations with line fit parameters are also included. Each bar is taken from roughly 100 data points.*

Figure 6.5a shows the bridge voltage output over a sweep of oxygen volume concentration. For this, the flow rate was set constant on the flow controllers, but their contributed ratio was changed differentially. The same measurement, but only with nitrogen gas, is shown in Figure 6.5b.

Comparison of the slopes with and without a magnet in Figure 6.5 shows for the case with oxygen a decrease of roughly 13%. The slopes with only N_2 gas show less than 1% change in slope with and without a magnet.

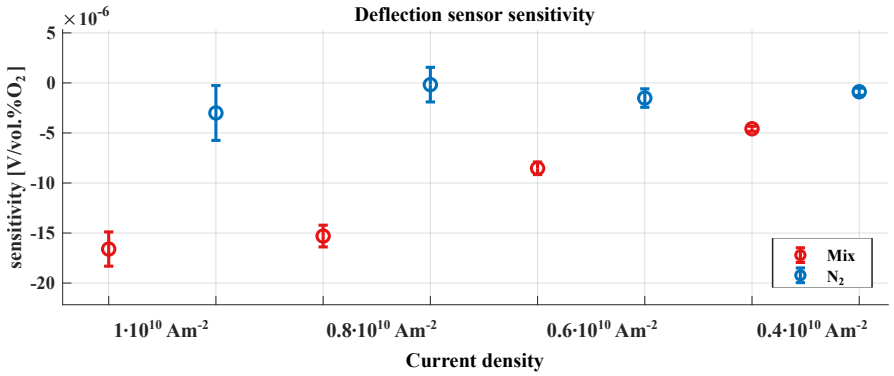

Figure 6.6: *The slope difference between with and without magnet with the standard error for a range of current densities. The colours indicate the gasses used in the flow rate fraction sweep between the flow controllers. Red indicates a mixture of air and nitrogen, and blue indicates only nitrogen.*

The measurement with only nitrogen indicates the sensor's flow dependence, unrelated to the oxygen concentration. In an attempt to negate this effect, slope differences were taken by subtracting the slope with and without a magnet. These are plotted for a range of current densities in Figure 6.6. The adjusted measurements show a low sensitivity for the case with only nitrogen. Increasing the current density, or temperature, of the calorimetric sensor also shows no significant increase of sensitivity compared to the case with oxygen. A higher current density also shows an increased standard error for the pure N_2 and mixture of gas case.

The flow rate dependency makes a straightforward step response in oxygen concentration challenging to interpret, as the flow rate change contributes to the signal. Therefore, it is left out of the results.

The observed flow rate dependency could be explained by an imbalance in flow rate between flow controllers. An estimated $83\,\mu m\,s^{-1}$ or roughly $30\,\mu L\,min^{-1}$ difference could have led to this slope, which lies within the expected accuracy deviation ($60\,\mu L\,min^{-1}$) of the flow controllers.

Looking at the adjusted measurement results, there is a small change in slope difference with and without a magnet for nitrogen compared to the mixture of gas. This indicates that the presence of a magnetic field shows a larger deflection in the side channel with oxygen.

Simulation comparison

Using the sensitivity found for the calorimetric flow sensors in Figure 6.4, with the sensitivities of $12\,Vm^{-1}s$ and $17\,Vvol.\%O_2^{-1}$ an estimated velocity of 1.4 $\mu m\,s^{-1}vol.\%O_2^{-1}$ can be derived. From the results found in [7] a similar estimated 1 to 10 $\mu m\,s^{-1}vol.\%O_2^{-1}$ can

be calculated assuming a flow sensor sensitivity of 1 to 10 $\mathrm{Vm}^{-1}\mathrm{s}$.

The velocities found from the simulations, however, are significantly higher. Some issues with the simulation have been found that explain this discrepancy. The simulation ignores the channel resistance. Viscous forces in the narrow channel are significant compared to the magnetic force. The resistance causes a buildup in the channel, dispersing more evenly among the side channels and decreasing the effect of deflection.

More importantly, the forced atmospheric pressure boundary condition on the channel outlets is invalid in combination with the volume force of the magnet. Around the magnet, an elevated pressure is observed due to the volume force. Placing a magnet close to a boundary condition of atmospheric pressure causes a pressure difference that results in an artificial flow from the increased pressure to the boundary atmospheric pressure. What this model does not capture is the extended volume force beyond the channel outlet. This causes the transition from the channel to atmosphere to be gradual beyond the outlet.

A model revision has been approached by moving the pressure boundary condition further from the outlets, similar to the simulation of the magnetic wind sensor. Channel resistance is better represented by including the channel height. The 3D geometry with the extended outlet boundary condition is shown in appendix A. The revised model shows a sensitivity of 18.5 $\mu\mathrm{m\,s}^{-1}\mathrm{vol.\%O_2^{-1}}$. The simulated sensitivity is closer to the measurement results but still 13 times larger.

6.3 Magnetic wind sensor

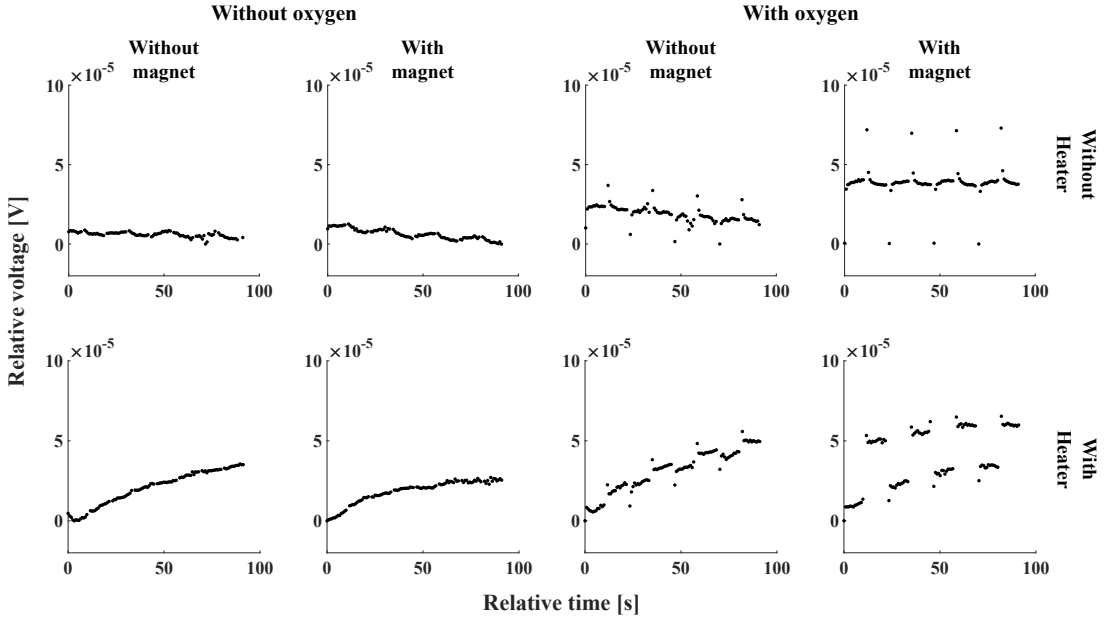

Figure 6.7: *Flow sensor voltage response to a square wave oxygen percentage signal between 4% and 16%. The time axis has been shifted to start at 0. The voltage axis is set to 0 for the minimum value of the measurement.*

Figure 6.7 shows the flow sensor voltage over time for different combinations of measurement parameters. For each plot, the flow controllers are switched between 20% and 80%

of the total flow rate of $10\,\mathrm{mL\,min^{-1}}$. The left two columns show the sensor response to nitrogen gas. There are bumps visible in the case when the heater is turned on. For the right two columns, the gas contains an alternating 4 to 16 vol.% oxygen. Compared to the case without oxygen, there are more outlying peaks when switching the flow rate between flow controllers. Both the cases with a heater, with and without a magnet, show a square wave response to the oxygen switching. however, the case with a magnet is roughly more than five times larger in voltage amplitude. The square wave response shows a response time faster than the sampling frequency of roughly 4 Hz.

Figure 6.8 shows the sensitivity of voltage per oxygen percentage change for magnet configurations. The slope with no magnet is negative, while the presence of a stack of two magnets shows an increased slope over the single magnet.

Figure 6.9 shows the sensitivity value with and without a heater in the case of one or two magnets. The sensitivity changes for increasing current density. For the case with the heat source turned on the sensitivity to oxygen increases with current density. The case without heater shows relatively stationary sensitivity over the same range. The addition of a second magnet shows an increased sensitivity for both with and without heater.

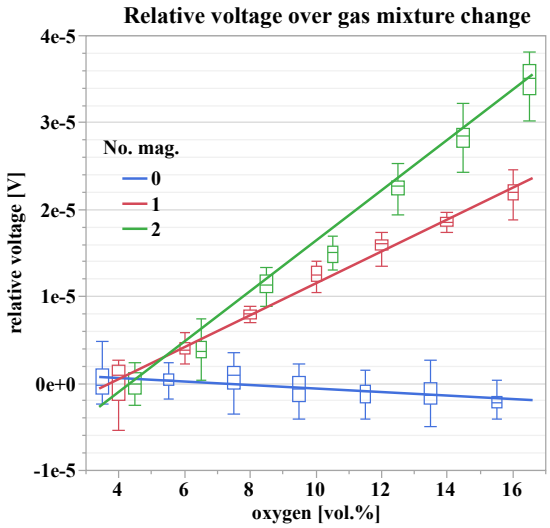

Figure 6.8: *Boxplots of the calorimetric voltage signal relative to the mean voltage at 4 vol.% oxygen over an increase in oxygen concentration for various magnet configurations.*

Figure 6.10a shows the voltage output of the flow sensor in the air with no gas from the inlet and with a single magnet. The measurements without magnets show a relatively consistent output signal. The same holds for the cases where the heater is turned on without a magnetic field. There is, however, a change in signal when the magnet is placed in different positions. Figure 6.10b plots the changes in flow sensor output with varying magnet positions where the measurements without magnet but with heater are taken as zero references. The plot shows that the sign of the flow signal changes when the magnet is changing sides with respect to the heater.

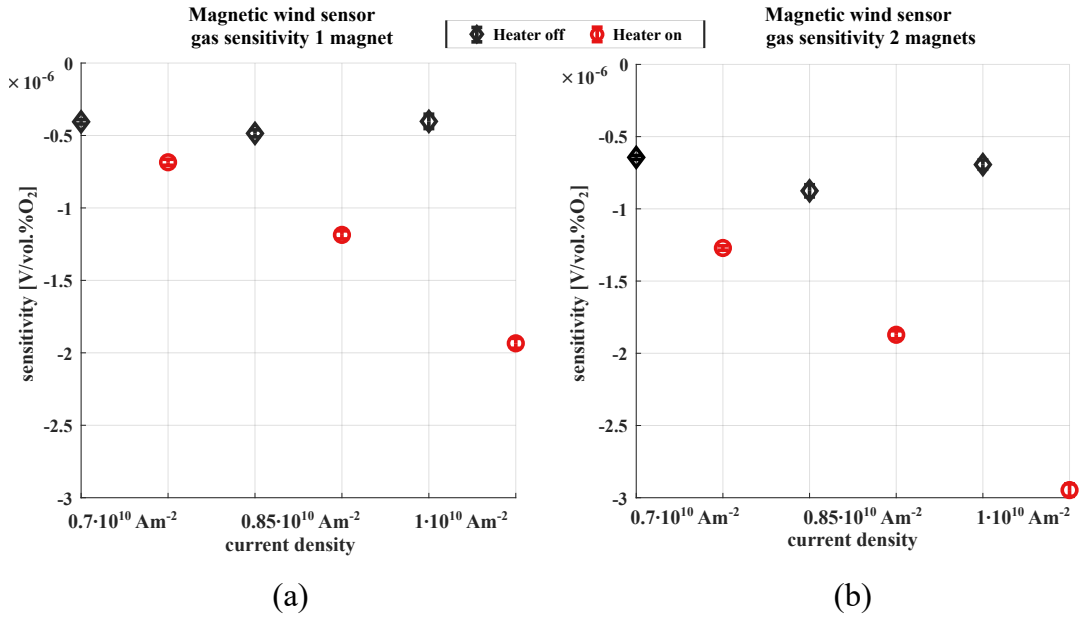

Figure 6.9: *Sensitivity of the flow sensor in voltage per oxygen percentage relative to the no magnet measurements showing the difference in the case with and without the heater turned on. Figures (a) and (b) show the case with 1 and 2 magnets, respectively, for various current densities over the Wheatstone bridge.*

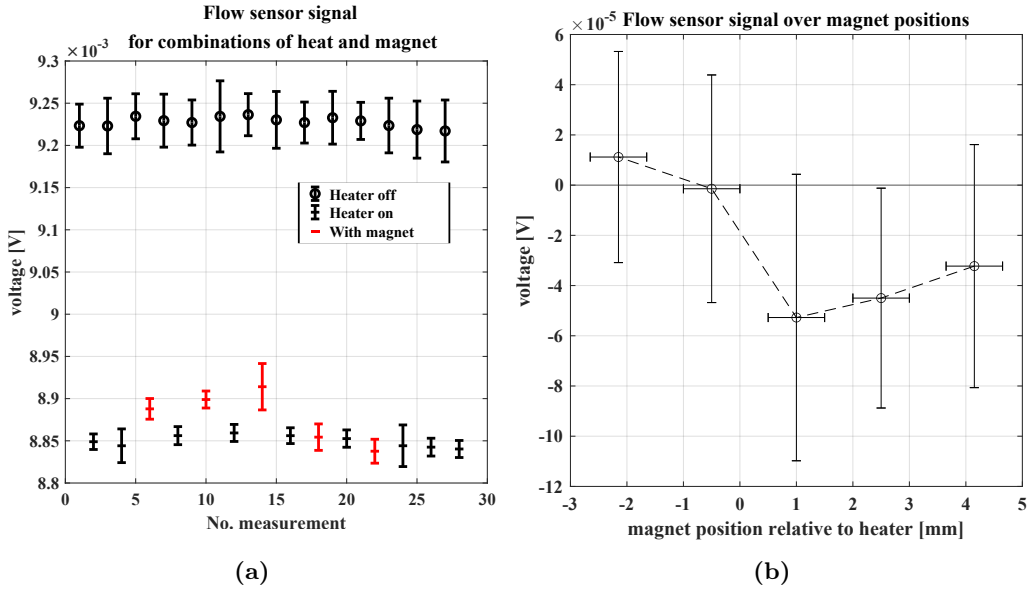

Figure 6.10: *(a) Flow sensor voltage output signal alternating with heater and various single magnet placements without gas from the inlet. (b) The flow sensor voltage signal changes for various positions of the magnet centre relative to the centre of the heater going from up to downstream. Vertical error bars indicate the standard error. Horizontal error bars are an estimation of the magnet placement accuracy by hand.*

The principle of magnetic wind is supported by the increased square wave response in the case of oxygen, magnet, and heater. Moreover, the change in flow direction was observed with no gas flow at the inlet.

Yet, there are responses in cases that can not be explained by magnetic wind. Figure 6.10 shows a persisting flow response in the case the heater is turned off. The reaction to the oxygen concentration does not change as much with an increasing current density as with the heater.

Possible flow rate dependency could result from asymmetries in the flow path on either side of the inlet. This could be a misalignment of tens of microns. Some mechanical deflection was observed in the heater mesh at 100 °C. This could have led to a change in channel resistance, contributing to the effect of the heater on the flow without a magnet.

Simulation comparison

Using the sensitivity for the calorimetric sensor of $16\,\mathrm{V\,m^{-1}\,s^{-1}}$ shows that the magnetic wind velocities were in the range of 1 to 10 $\mu\mathrm{m\,s^{-1}}$. Compared to the simulation, the velocity range is off by roughly two orders of magnitude. The difference could be due to incorrect modelling of the temperature dependency of the susceptibility value. The unexpected flow responses in the cases without oxygen or a heater are also not reflected in the simulations. In spite of this, the simulation shows qualitative similarities in the behaviour of magnetic wind by capturing the change in flow direction and magnitude depending on the magnet position.

6.4 Conclusion

This chapter has presented an experimental characterization and analysis of the flow sensor prototypes of the deflection-based sensor and magnetic wind sensor. The initial characterization of the calorimetric flow sensor showed its sensitivity and some indication of its dependence on sensor geometry. Comparing the results deviated from the analytical models, and these discrepancies highlighted areas needing further refinement, such as accounting for likely missing heat loss components.

The deflection sensor showed a large sensitivity to flow rate changes. Adjusting for these deviations, a sensitivity of 1.4 $\mu\mathrm{m\,s^{-1}vol.\%O_2^{-1}}$ or 17 $\mu\mathrm{Vvol.\%O_2^{-1}}$ was found. Problems with the simulation were found in neglecting the channel resistance and incorrect use of boundary conditions. However, the new simulation still deviated from the measurements.

The magnetic wind sensor showed a sensitivity of 3 $\mu\mathrm{Vvol.\%O_2^{-1}}$. The behaviour with magnet position also showed similarities with the simulations. However, the simulation values were significantly off, and sensitivity to oxygen was also observed in the case with no heater, which could not be explained.

Chapter 7

Conclusion

This thesis has contributed to the development of MEMS-based paramagnetic oxygen sensors by providing a proof of concept that leverages existing sensing principles, including magnetic wind and paramagnetic deflection. The primary aim was to design, simulate, and fabricate prototype MEMS paramagnetic oxygen sensors capable of detecting oxygen concentrations between 0-20 vol.% with high sensitivity and fast response times.

The experimental results from the fabricated prototypes indicate the feasibility of the magnetic wind and deflection-based sensing approaches. Discrepancies were observed compared to the simulation predictions. These discrepancies highlighted areas requiring further refinement. Issues with FEM simulations for the deflection sensor were found and addressed with an adjusted model. Even though the FEM models for both sensor types show comparable trends in behaviour, they still deviate more than one order of magnitude.

Indirect measurements of the performance of the deflection sensor yield an estimated sensitivity of 17 µVvol.%O_2^{-1}. The results from the magnetic wind sensor indicate the presence of magnetic wind with an estimated sensitivity of 3 µVvol.%O_2^{-1}. However, some sensor reactions remain unexplained.

Overall, this work showed proof-of-concept devices that demonstrated sensitivity to changes in oxygen concentration. While the target specifications for accuracy (0.1 vol.%) and response time (<1 s) were not verifiable with direct measurements, the findings provide a foundation for continued optimization and development.

7.1 Outlook

The main issues in both sensors that need to be addressed are the flow rate and temperature dependency. The flow rate dependency could be addressed using a secondary flow sensor at the inlet. The two flow sensors could then possibly be integrated into a full Wheatstone bridge. Proper annealing steps can reduce temperature drift. A separate temperature sensor could also track and compensate for the bulk temperature.

Improvements in the fabrication process can be made in the metal deposition. Instead of the lift-off method, a self-aligned process can be used. This would further reduce heat losses to the substrate and ear formation. Improvements in sensor assembly can also help the alignment of the chip halves that cause asymmetries in the channels.

Further efforts are needed in the theoretical understanding to improve the alignment of models and simulation approaches with experimental observations. The bases for the COMSOL model could be used to test and explore novel geometries or other paramagnetic sensor concepts. Improving the thermal flow sensor model could help find a better design with improved sensitivity.

Bibliography

[1] James A Jahnke. *Continuous emission monitoring*. John Wiley & Sons, 2022.

[2] R Ramamoorthy, PK Dutta, and SA Akbar. Oxygen sensors: materials, methods, designs and applications. *Journal of materials science*, 38:4271–4282, 2003.

[3] Michela Quaranta, Sergey M Borisov, and Ingo Klimant. Indicators for optical oxygen sensors. *Bioanalytical reviews*, 4:115–157, 2012.

[4] Krzysztof Jasek, Mateusz Pasternak, and Michał Grabka. Paramagnetic sensors for the determination of oxygen concentration in gas mixtures. *ACS sensors*, 7(11):3228–3242, 2022.

[5] General Electric Company. *XMO2-IDM Oxygen Analyser User's Manual*, f edition, October 2013.

[6] U Schmid, H Seidel, G Mueller, and Th Becker. Theoretical considerations on the design of a miniaturised paramagnetic oxygen sensor. *Sensors and Actuators B: Chemical*, 116(1-2):213–220, 2006.

[7] Stefan Vonderschmidt and Jörg Müller. A fluidic bridge based mems paramagnetic oxygen sensor. *Sensors and Actuators B: Chemical*, 188:22–30, 2013.

[8] P Krippner, M Wetzko, P Szasz, B Andres, and T Bauer. Mems based paramagnetic oxygen measurement. In *TRANSDUCERS 2007-2007 International Solid-State Sensors, Actuators and Microsystems Conference*, pages 2393–2396. IEEE, 2007.

[9] J.M.D. Coey. *Magnetism and Magnetic Materials*. Magnetism and Magnetic Materials. Cambridge University Press, 2010.

[10] Bernard Dennis Cullity and Chad D Graham. *Introduction to magnetic materials*. John Wiley & Sons, 2011.

[11] Jun Cai, Li Wang, Ping Wu, Zhengqiang Li, Lige Tong, and Shufeng Sun. Study on oxygen enrichment from air by application of the gradient magnetic field. *Journal of Magnetism and Magnetic Materials*, 320(3-4):171–181, 2008.

[12] Nicolae Damean, Paul PL Regtien, and Miko Elwenspoek. Heat transfer in a mems for microfluidics. *Sensors and Actuators A: Physical*, 105(2):137–149, 2003.

[13] H H Bruun. Hot-wire anemometry: Principles and signal analysis. *Measurement Science and Technology*, 7, 1996.

[14] Theodore L Bergman, Adrienne S Lavine, Frank P Incropera, and David P DeWitt. *Introduction to heat transfer*. John Wiley & Sons, 2011.

[15] Louis Vessot King. On the convection of heat from small cylinders in a stream of fluid: Determination of the convection constants of small platinum wires, with applications to hot-wire anemometry. *Proceedings of the Royal Society of London. Series A, Containing Papers of a Mathematical and Physical Character*, 90(622):563–570, 1914.

[16] Hans-Elias De Bree, Henri V Jansen, Theo SJ Lammerink, Gijs JM Krijnen, and Miko Elwenspoek. Bi-directional fast flow sensor with a large dynamic range. *Journal of micromechanics and microengineering*, 9(2):186, 1999.

[17] Cameron Tropea, Alexander L Yarin, John F Foss, et al. *Springer handbook of experimental fluid mechanics*, volume 1. Springer, 2007.

[18] Theo SJ Lammerink, Niels R Tas, Miko Elwenspoek, and Jan HJ Fluitman. Micro-liquid flow sensor. *Sensors and actuators A: Physical*, 37:45–50, 1993.

[19] B Puers and Willy Sansen. Compensation structures for convex corner micromachining in silicon. *Sensors and Actuators A: Physical*, 23(1-3):1036–1041, 1990.

[20] Matthias Thiele and Jens Lienig. *Fundamentals of Electromigration-Aware Integrated Circuit Design*. Springer International Publishing, 2018.

[21] Shirin Azadi Kenari, Remco J Wiegerink, Henk-Willem Veltkamp, Remco GP Sanders, and Joost C Lötters. Thermal flow meter with integrated thermal conductivity sensor. *Micromachines*, 14(7):1280, 2023.

[22] Mattias Vangbo and Ylva Baecklund. Precise mask alignment to the crystallographic orientation of silicon wafers using wet anisotropic etching. *Journal of Micromechanics and Microengineering*, 6(2):279, 1996.

[23] Edwin Acosta. Thin films/properties and applications. In *Thin Films*. IntechOpen, 2021.

[24] Supermagnete. Questions and answers about the grade of magnets. `https://www.supermagnete.nl/eng/faq/Questions-and-answers-about-the-grade-of-magnets`, n.d. Accessed: Aug. 24, 2024.

[25] K Tsutsumi, A Yamashita, and H Ohji. The experimental study of high tcr pt thin films for thermal sensors. In *SENSORS, 2002 IEEE*, volume 2, pages 1002–1005. IEEE, 2002.

[26] Yujia Zhai, Changlong Cai, Jing Huang, Huan Liu, Shun Zhou, and Weiguo Liu. Study on the resistance characteristic of pt thin film. *Physics Procedia*, 32:772–778, 2012.

[27] Xiaoman Wang, Rulei Guo, Qinping Jian, Guilong Peng, Yanan Yue, and Nuo Yang. Thermal characterization of convective heat transfer in microwires based on modified steady state" hot wire" method. *arXiv preprint arXiv:1907.10751*, 2019.

[28] Raghu Pulavarthy. Characterization of heat transfer coefficient at micro/nano scale and the effect of heated zone size. 2015.

[29] Fukang Jiang, Yu-Chong Tai, Chih-Ming Ho, and Wen J Li. A micromachined polysilicon hot-wire anemometer. In *Solid-State Sensor and Actuator Workshop*, pages 264–267, 1994.

Appendix A

Simulations

Volume force

The implemented volume force that has been applied to the laminar flow part of the simulation:

```
Fx = d(mfnc.BX^2+mfnc.BY^2+mfnc.BZ^2,x) * po2 * 6.88e-7  * ...
    (293^2 / T^2) /(mu0_const*2)
Fy = d(mfnc.BX^2+mfnc.BY^2+mfnc.BZ^2,y) * po2 * 6.88e-7  * ...
    (293^2 / T^2) /(mu0_const*2)
Fz = d(mfnc.BX^2+mfnc.BY^2+mfnc.BZ^2,z) * po2 * 6.88e-7  * ...
    (293^2 / T^2) /(mu0_const*2)
```

Boundary conditions

Figure A.1 shows the geometry used for the simulation of the deflection and magnetic wind sensor. The physical sensor outlets are connected to a large volume that acts as an outside environment. The back wall of this volume is set to atmospheric pressure.

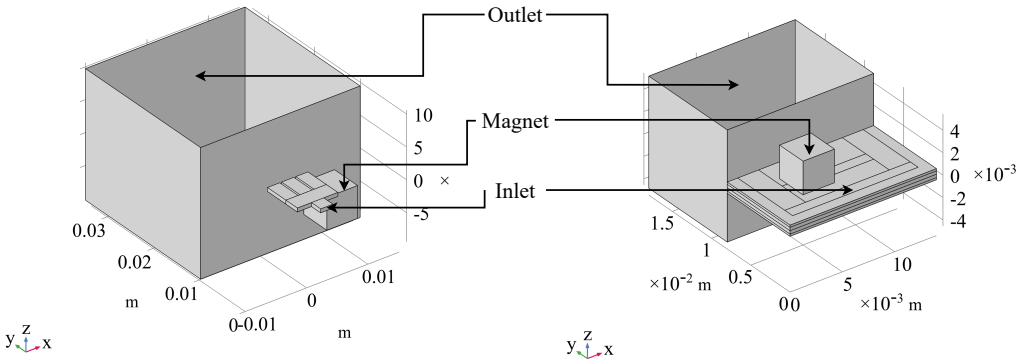

Figure A.1: *The geometries of the (l) deflection of flow and (r) magnetic wind sensor used in COMSOL. Indicated by arrows are the outlet, inlet, and magnet.*

Appendix B

Fabrication

The sensors were fabricated at the MESA+ Nanolab at the University of Twente.

525 ± 5 µm silicon p-doped substrates where used.

B.1 Lithography

All lithography steps were performed using the *MLA 150* from *Heidelberg Instruments*. The correct exposure and defocus settings required a calibration test, as the thickness of the transparent SiRN can cause thickness-specific backscattering. Using the test patterns, as shown in Figure B.1b, and sweeping over exposure parameters, an exposure of 140 $\mathrm{mJ\,cm^{-2}}$ and a defocus of 0 has been found to yield the highest resolution. Features down to 1 µm could be defined. These parameters were both used for the *Olin-17* and *AZ-3012* resist.

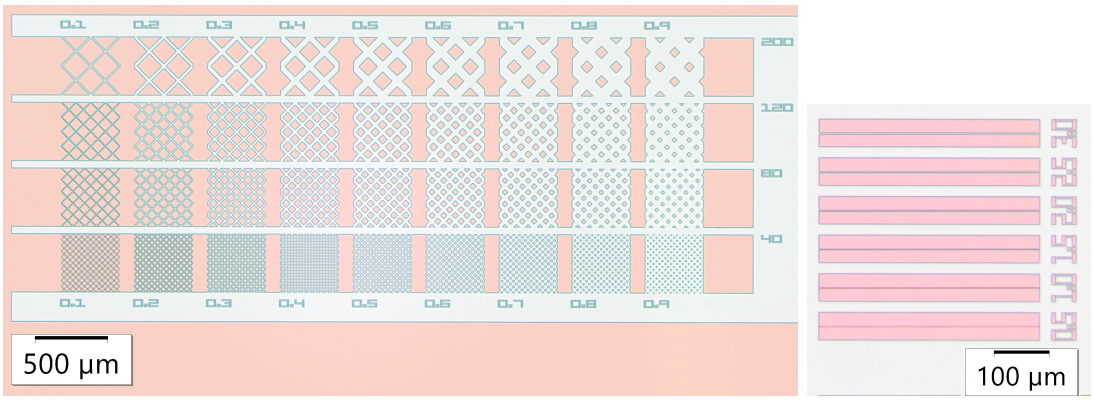

(a) **(b)**

Figure B.1: *Different test structures for finding the correct exposure parameters showing (a) a test pattern containing mesh structures and (b) various thin wire widths. In white SiRN and in pink photoresist.*

B.2 Etching test structures

A test mask was used to test various overhanging SiRN structures and the etching of KOH. Figure B.2 shows the test of the compensation structure, and Figure B.3 shows the etching test of various mesh geometries. Green in these images shows the SiRN film on silicon, light pink shows the overhanging structures, and dark grey to black shows the underlying silicon.

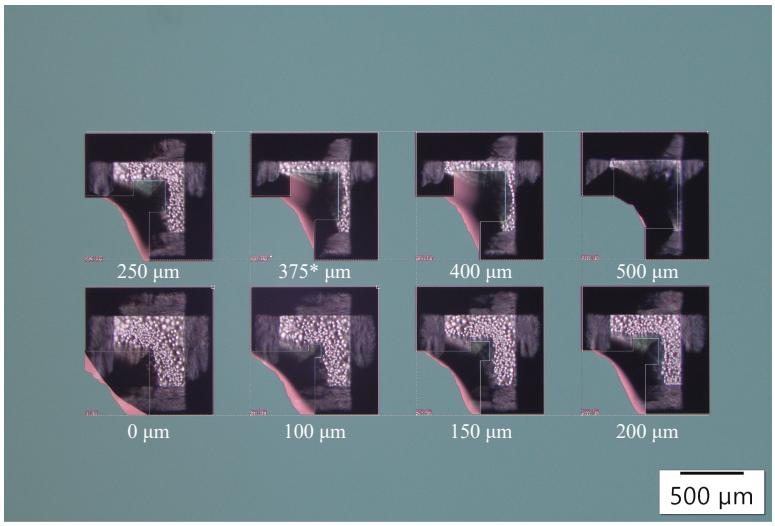

Figure B.2: *Range of square corner compensation structures with the sizes.*

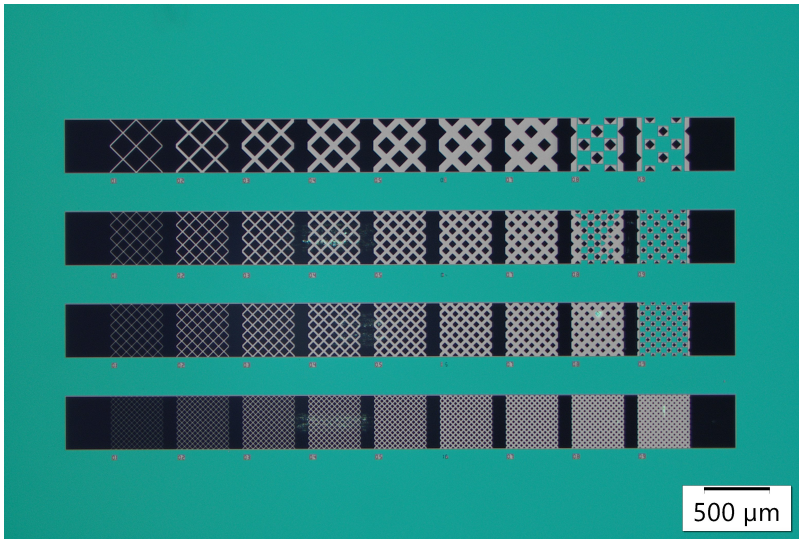

Figure B.3: *Mesh sizes [200, 100, 80, 40]* µm *from top to bottom and ratios of a/A of 0.1 to 0.9 with 0.1 increment steps from left to right.*

B.3 Process outline

Table B.1: *Process sheet of a single-sided process*

Step	Process	Process parameters	Remarks
1	Select wafer	- Orientation: ⟨100⟩ - Diameter: 100 mm - Thickness: 525 µm ± 25 µm - Double side polish	
		Vangbo allignment	
2	Preperation LPCVD cleaning	- HNO_3 99% 5 min - Quick dump rinse - HNO_3 99% 5 min - Quick dump rinse - HNO_3 69% 10 min 96 °C - Quick dump rinse - Spin dry	
3	Preperation LPCVD native oxide strip	- HF 1% 1 min - Quick dump rinse - Spin dry	
4	LPCVD low stress SiRN	- Tempress LPCVD furnace - Thickness: 150 nm - Duration: 23 min - Temperature: 850 °C - Pressure: 150 mTorr - SiH_2Cl_2 flow: 72 sccm - NH_3 flow: 22 sccm - N_2 flow: 150 sccm	
5	Litography	- MLA150 - Dehydration bake 120 °C 5 min - HMDS priming - 4000 rmp 30 s - Olin resist 17 µm - 4000 rmp 30 s - Prebake 95 °C 90 s - Allignment - Exposure - 140 mJ cm^{-2} 0 defocus - Postbake 120 °C 60 s - Development OPD4262 - Quick dump rinse - Spin dry	Vangbo mask

Table B.1 continued from previous page

Step	Process	Process parameters	Remarks
6	Directional RIE of SiRN	- PT790 - Etch speed: 40 nm/min - 2x 2.5 min with 180 deg rotation	
7	Resist strip	- TePla360 - O_2 plasma - 30 min	
8	Preperation KOH native oxide strip	- HF 1% 1 min - Quick dump rinse - Spin dry	
9	KOH etch	- KOH 25 w.% - Temperature: 75 °C - 15 min - RCA-2 cleaning	
	Lift off metal		
10	Preperation LPCVD	- HNO_3 99% 5 min - Quick dump rinse - HNO_3 99% 5 min - Quick dump rinse - HNO_3 69% 10 min 96 °C - Quick dump rinse - Spin dry	
11	LPCVD low stress SiRN	- Tempress LPCVD furnace - Thickness: 500 nm - Duration: 1.5 h - Temperature: 850 °C - Pressure: 150 mTorr - SiH_2Cl_2 flow: 72 sccm - NH_3 flow: 22 sccm - N_2 flow: 150 sccm	

Table B.1 continued from previous page

Step	Process	Process parameters	Remarks
12	Litography	- MLA150 Heidelberg instruments - Dehydration bake 120 °C 5 min - HMDS priming - 4000 rmp 30 s - AZ 3001 resist - 4000 rmp 30 s - Prebake 95 °C 90 s - Allignment - Exposure - 140 mJ cm^{-2} 0 defocus - Postbake 120 °C 60 s - Development OPD4262 - Quick dump rinse - Spin dry	Metal mask
13	Evaporation Cr/Pt	- TOPdamper (custom design) - 10 nm Cr - 100 nm Pt	
14	Resist stripping	- Ultrasonic bath - Acetone VSLI - 30 min	
		Single sided KOH etching	
15	Litography	- MLA150 Heidelberg instruments - Dehydration bake 120 °C 5 min - HMDS priming - 4000 rmp 30 s - Olin resist 17 µm - 4000 rmp 30 s - Prebake 95 °C 90 s - Allignment - Exposure - 140 mJ cm^{-2} 0 defocus - Postbake 120 °C 60 s - Development OPD4262 - Quick dump rinse - Spin dry	SiRN KOH window front mask

Table B.1 continued from previous page

Step	Process	Process parameters	Remarks
16	IBE	- SCIA Mill 150 - Power: 250 W - Ion beam source voltage: 400 V - Ion beam accelerator voltage: 300 V - Neutralizer emission current: 250 mA - Ion beam argon flow: 15 sccm - Neutralizer argon flow: 7 sccm - Process pressure: 7e-4 mbar - Chuck rotation: 10 rpm - Angle of incidence: -20 deg - Etch time 17 min	Performed in Delft Alternatively RIE would also work
17	KOH etch	- KOH 25 w.% - Temperature: 75 - 5 h - Quick dump rinse - Spin dry	

Table B.1 gives an overview of the process outline listing important process parameters. The outline only describes the patterning of the hard mask of one side of the wafer.

B.4 Photomasks

A positive photoresist is used, and the masks are represented in negative, meaning that the photoresist will be exposed in the black parts.

The SiRN alignment marks for the magnet on the TMW chip on the back are too far towards the middle of the chip; they are not correctly aligned with the front metal mark.

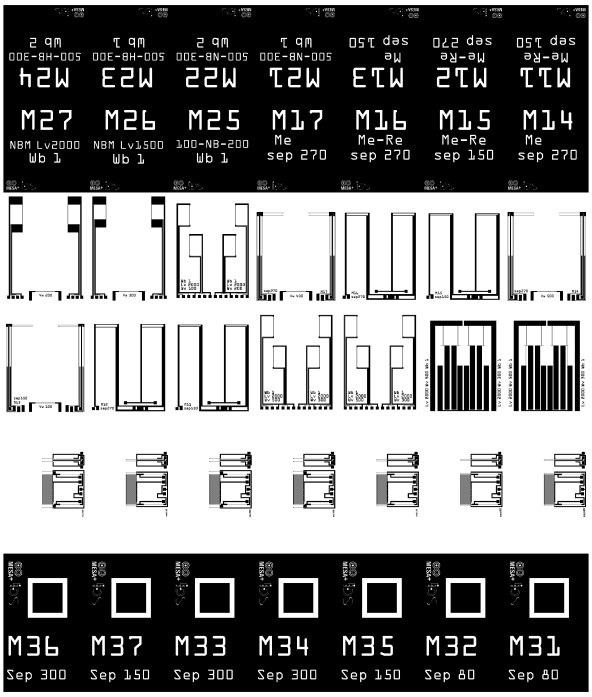

Figure B.4: *Negative photomask of the metal layers, where black will be exposed.*

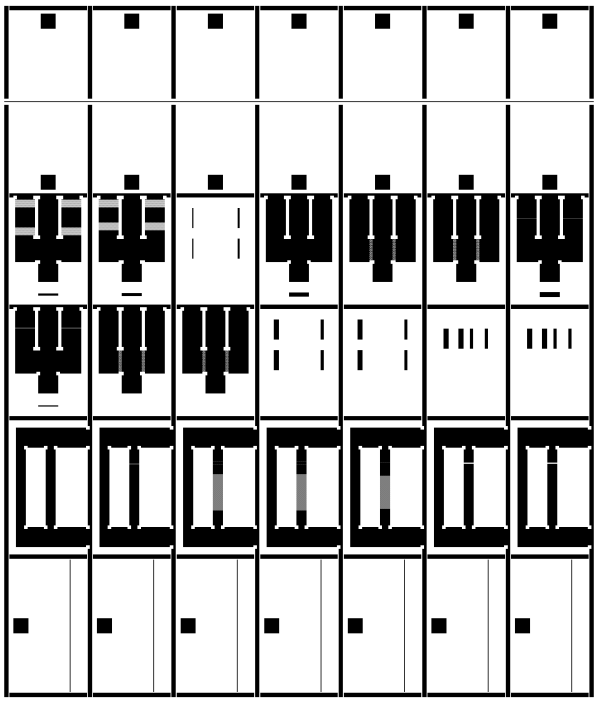

Figure B.5: *SiRN frontside window negative photomask.*

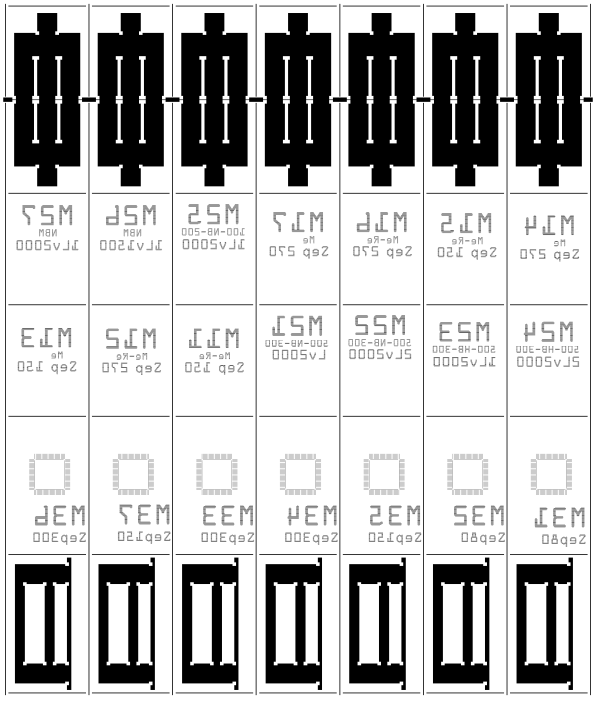

Figure B.6: *SiRN backside window negative photomask.*